Trigger Implementation for FAMOUS

von

Alexander Bogner

Bachelorarbeit in Physik

vorgelegt der
Fakultät für Mathematik, Informatik und Naturwissenschaften
der
Rheinisch Westfälischen Technischen Hochschule Aachen

im Oktober 2016

angefertig am

III. Physikalischen Institut A

Erstgutachter und Betreuer

Jun. Prof. Dr. Thomas Bretz
III. Physikalisches Institut A
RWTH Aachen

Zweitgutachter

Prof. Dr. Thomas Hebbeker
III. Physikalisches Institut A
RWTH Aachen

Contents

1. Introduction

The existence and investigation of air showers has interested mankind for many decades. To detect air showers photo-multiplier tubes have been established and used in the world largest observatory examining air showers, the Pierre Auger Observatory. The FAMOUS telescope instead utilises SiPMs, which are compact and low voltage semiconducting devices able to detect single photons.
In order to read out the data that the 64 SiPMs of the FAMOUS telescope provide, a new data acquisition namely TARGET had to be put in operation. Therefore trigger groups (à four pixels) have to be chosen since the TARGET data acquisition triggers only when the sum of four channels, where each channel represents a pixel of the FAMOUS telescope, reaches a certain threshold. Consequently, a satisfying layout, that meets several requirements is needed. Therefore three layouts were created and their geometrical properties were examined and corresponding to their advantages and disadvantages weighted. Moreover a simulation which allows even further examination of the different layouts provided the last criteria for choosing the most efficient layout. Based on this layout a PCB had to be designed, which uses the pixel allocation as prescribed by the layout. The PCB routs the incoming signal, which is provided by two 70-pin header onto four 26-pin connectors.
With the help of this PCB the TARGET data acquisition is made completely operational and the SiPM data of all 64 SiPMs can be read out and analysed. Furthermore the internal trigger of the TARGET module can be utilised.

2. Cosmic rays

The discovery of an increase of flux with increasing altitude by Victor Hess in 1912 [1] was the beginning of cosmic ray experiments since the increased flux could not be explained by radioactive materials in the Earth. Further researches where done by Pierre Auger in 1939. His conclusion was that the measured fluxes can be derived as interactions between primary cosmic rays (with extraterrestrial origin) and the atmosphere [2].

2.1 Energy spectrum

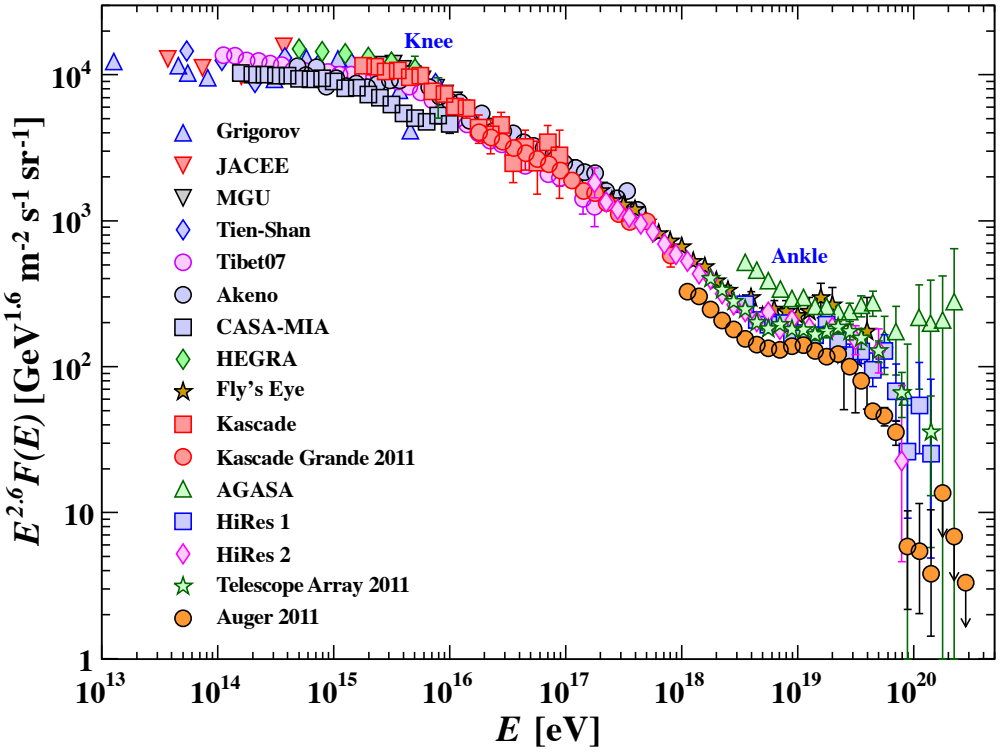

Figure 2.1: The all-particle spectrum as a function of E which was determined by indirect detection methods. The flux has been multiplied by $E^{2.6}$ to enhance the visibility of the steep spectrum (between 10^{15} and 10^{16} eV) features. Taken from [3]

The all-particle spectrum is shown in figure 2.1, whereas the energy spectrum has been multiplied by $E^{2.6}$ so that the features of the steep spectrum are visible.

The flux can be approximated by a broken power law $\propto E^{\gamma}$ with a spectral index $\gamma = -2.7$ for energies below $E \approx 4{*}10^{15}\,\mathrm{eV}$. For energies higher than $E \approx 4{*}10^{15}\,\mathrm{eV}$ (commonly known as the knee) the spectral index changes to $\gamma \approx -3.1$ and at energies of $5 * 10^{15}\,\mathrm{eV}$ the flux reaches $\gamma \approx -2.6$ [4]. At even higher energies of about $10^{20}\,\mathrm{eV}$ the spectrum reaches a certain limit, which could possibly be explained by the slowing-interactions of cosmic ray protons with the microwave background radiation which limit the flux to a certain level, also known as GZK limit [5].

2.2 Extensive air showers

Extensive air shower (EAS) are interactions between primary particles, which enter the Earth's atmosphere and air molecules, such as nitrogen and oxygen. During these interactions various secondary particles (electrons, muons and hadrons) are created. They themselves lose energy causing electromagnetic, muonic and hadronic cascades. Electromagnetic showers are initiated by photons or electrons and lose energy by particle production processes, bremsstrahlung of electrons, ionization and pair production. The total energy loss can be described by [4]:

$$\frac{\mathrm{d}E}{\mathrm{d}X} = -\alpha(E) - \frac{E}{X_R} \tag{2.1}$$

$\alpha(E)$ describes the ionization energy loss (Bethe-Bloch formula) and X_R the radiation length, which depends on the material a shower expands in [4]. The electromagnetic shower properties can be understood using der Heitler model [6]. Whereas hadronic showers can be characterized with help of the Gaisser-Hillas function [7], which describes the longitudinal particle density of an EAS:

$$N(X) = N_{\max}\left(\frac{X - X_0}{X_{\max} - X_0}\right)^{\frac{X_{\max}-X_0}{\lambda}} \exp\left(\frac{X_{\max} - X}{\lambda}\right). \tag{2.2}$$

Here $N(X)$ represents the number of particles as a function of the traversed atmospheric depth X and $N_{\max}$ identifies the maximum number of particles at3 the atmospheric depth $X_{\max}$. X_0 and λ are primary mass and energy dependent parameters [7].

2.3 Air-Cherenkov radiation

The detection of Cherenkov light is particularly interesting for observation of high-energy photons or cosmic rays because of the possibility to determine the direction and energy. Cherenkov light is emitted when secondary particles, from interaction between charged cosmic rays and the earth's atmosphere [9], travel through a dielectric medium with a speed greater than the phase velocity of the light in that medium ($v \geq c/n$) [10]. Aslong as the particle moves slower than the light speed in the corresponding medium the emitted waves interfere destructively and no Cherenkov light can be observed. For speeds greater than the light speed the emitted radiation is orientated along a cone whose opening angle is described by $\cos(\theta) = (n\beta)^{-1}$. Where n indicates the refractive index and β represents the relativistic beta. Figure 2.3 shows the typical spherical wave fronts as a result of the Cherenkov radiation.

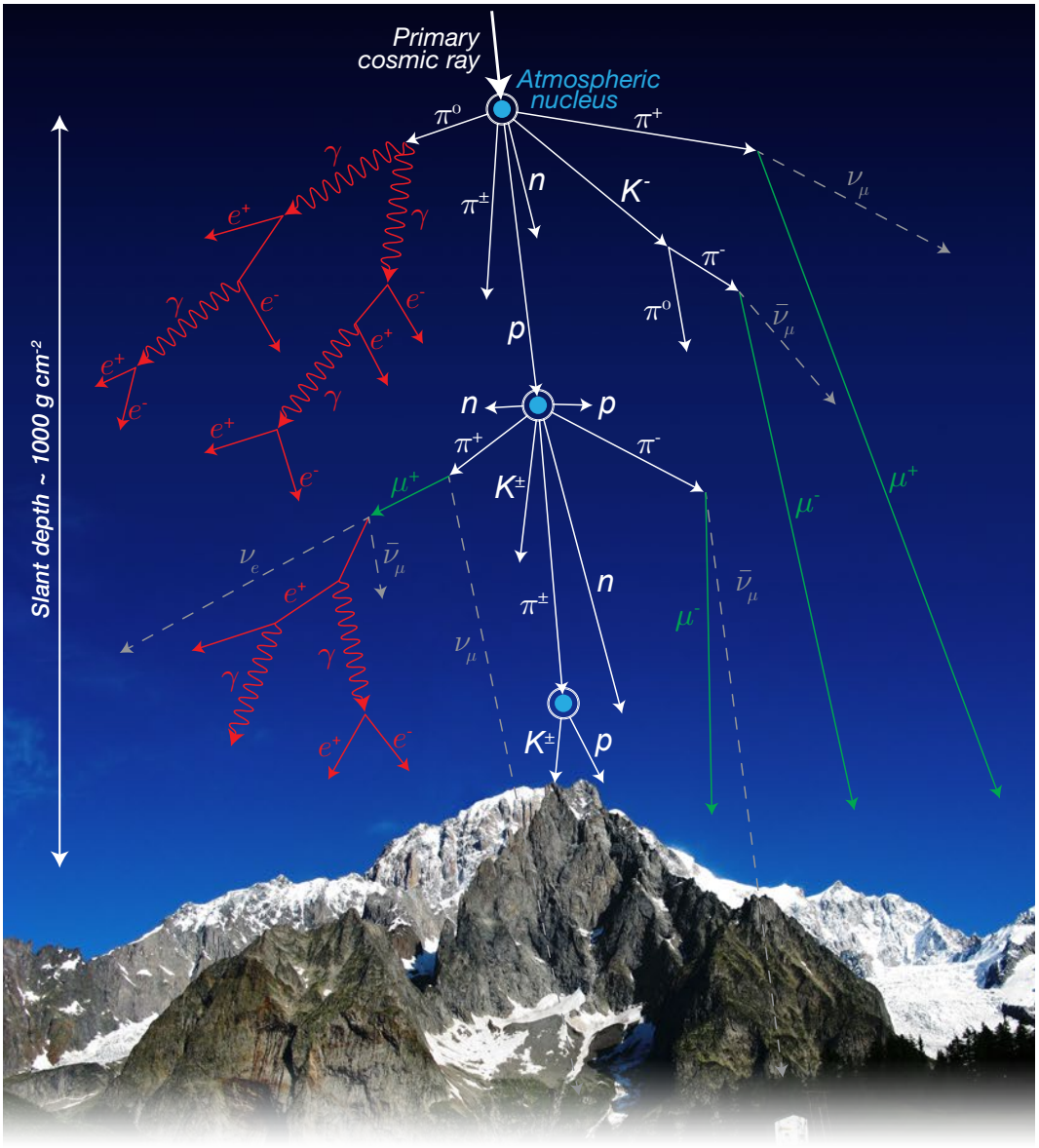

Figure 2.2: Illustration of a primary particle collision with the atmosphere and the subsequent cascades due to the collision. Taken from [8]

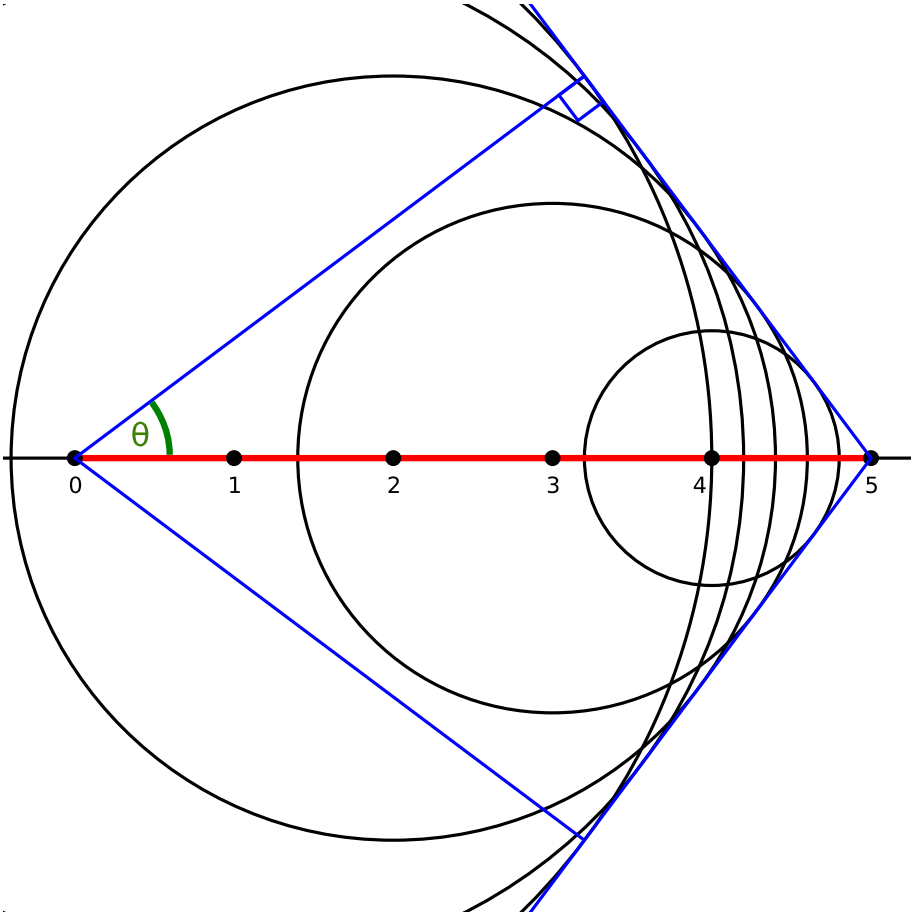

Figure 2.3: Schematic of Cherenkov radiation for a charged particle with $1/n\beta = 0.8$. Adapted from [11]

2.4 Pierre Auger Observatory

The Pierre Auger Observatory which is located in the Argentinian Pampa Amarilla is the world largest air shower observatory with a detection area of $3,000\,\mathrm{km}^2$. The observatory itself consists of 1660 surface detector tanks (SD) and 27 atmospheric fluorescence detector telescopes (FD). The surface detector stations are water tanks filled with $12,000$ liter purified water. Within those tanks three photomultipliers are able to detect Cherenkov light. The fluorescence detectors are placed at four observation sites (Los Leones, Los Morados, Loma Amarilla and Coihueco). The detectors consist of an aperture system with a diameter of 2.2 m and 37 mirror segments which are arranged into a spherical mirror system with a curvature of 3.5 m. Inside the focal plane a camera is mounted which consists of 440 photomultipliers which are arranged into a hexagonal grid in order to achieve a field of view of $30\,^\circ$ resulting in a total field of view of $180\,^\circ$ azimuth [12]. Schematics of the construction can be found in Figure 2.5.

Figure 2.6 shows a map of the Pierre Auger Observatory. The grey dots represent the position of the surface detectors and the blue lines the field of view of all fluorescence telescopes which are located at the four observation sites.

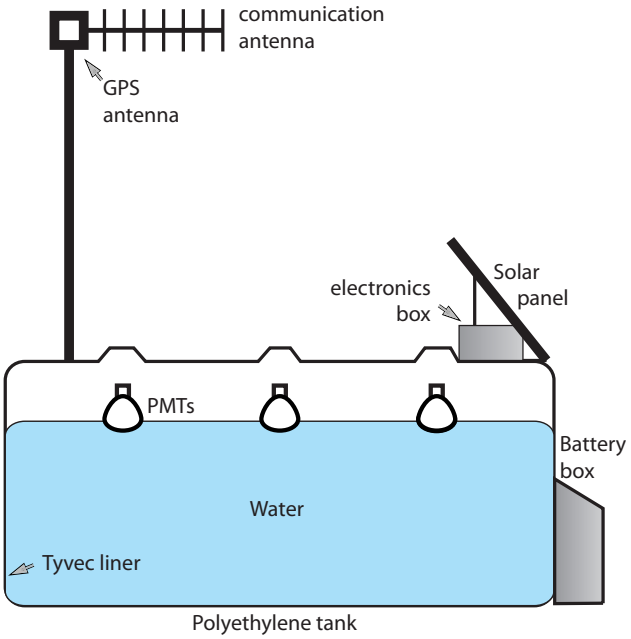

Figure 2.4: Scheme of a surface detector used at the Pierre Auger Observatory. Taken from [13].

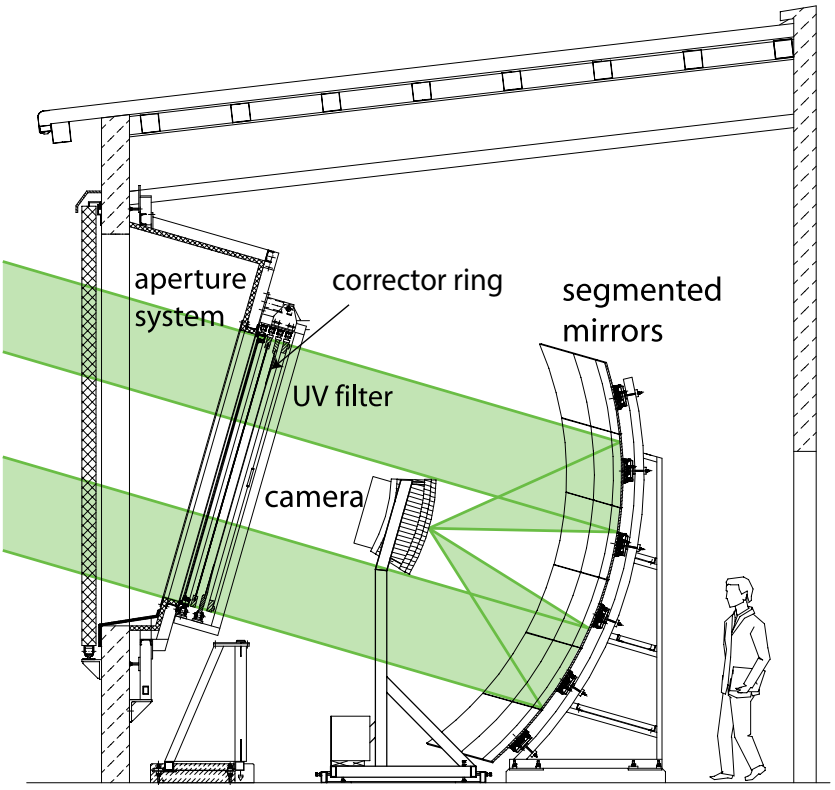

Figure 2.5: Shematic view of a fluorescence detector telescope. Adapted from [8].

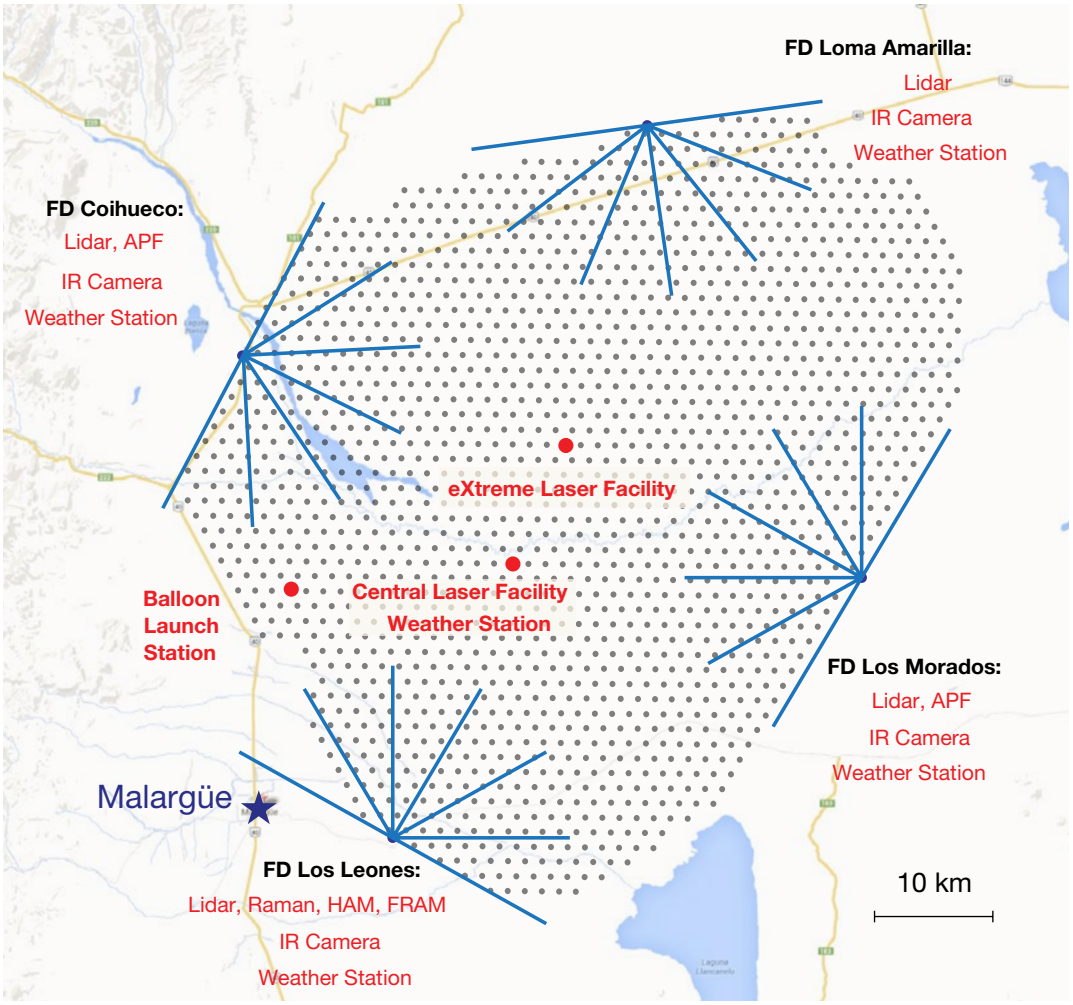

Figure 2.6: Map of the entire area used for the detection of air showers. The gray dots serve as illustration for the surface detectors and the red dots show the position of site where other experiments are carried out. The blue lines represent the field of view of each fluorescence detector. Taken from [8].

3. The FAMOUS Telescope

FAMOUS (**F**irst **A**uger **M**ulti-pixel photon counter camera for the **O**bservation of **U**ltra-high-energy cosmic air **S**howers) is a fluorescence detector which uses 64 SiPMs (silicon photomultipliers) to measure fluorescence light emitted by extensive air showers. The overall goal is to proof that SiPMs are suited for the efficient detection of air showers since SiPMs promise to be more effective than the established PMTs (photomultiplier tubes) in many ways (see section 3.2).

3.1 Baseline Design

The telescope itself consists of a Fresnel lens with a diameter of $d = 549.7\,\mathrm{mm}$, a focal length of $f = 502.1\,\mathrm{mm}$ and 10 grooves per millimeter [14]. The lens focuses the light on the focal plane where 61 pixels are arranged into a hexagonal grid. Each pixel consists of an array of four $3 \times 3\,\mathrm{mm}^2$ SiPM and a UV-pass filter which are mounted behind a Winston cone. Winston cones maximise the sensitive area while minimising the share of dead area. Each pixel has a field of view of $1.5^\circ \times 1.5^\circ$ resulting in a total field of view of about $12^\circ \times 12^\circ$. This allows detection of Cherenkov and fluorescence shower caused by extensive air showers. Schematics of the design of the FAMOUS telescope can be found in Figure 3.1, which shows the dimensions of the telescope and the setup of one pixel.

3.2 Silicon Photomultipliers

Silicon photomultipliers (SiPM) are single photon sensitive detection devices which contain an array of avalanche photodiodes which are operated in Geiger-mode (G-APD). An avalanche photodiode (APD) is a semiconductor which amplifies the signal created by incoming photons that cause electron-hole-pairs with gains up to 500. This is reached by p- and n-doped regions which are brought together to create a pn-junction that in turn creates a depletion zone. By applying reverse bias voltages V_{bias}, lower than the breakdown voltage, the (photo)electrons drift into the transition region. Within this region the electrons are accelerated into various directions and induce secondary electrons through impact ionization. The avalanche is caused by electrons running through the same process over and over again. To reach even higher gains of up to 10^6 the bias voltage has to be increased to a level that is slightly higher than the breakdown voltage, because the gain has a strong dependence of the applied field strength.

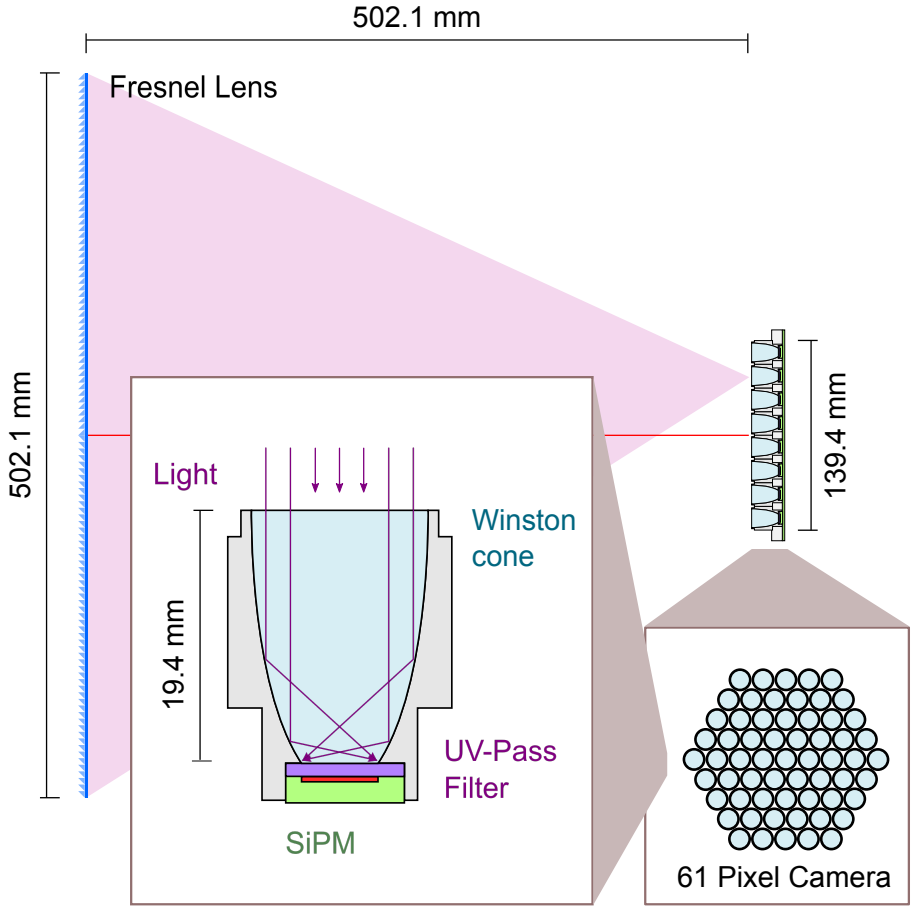

Figure 3.1: Schematic of the baseline design of FAMOUS. Adapted from [15].

APDs operated with a bias voltage above the breakdown voltage are commonly referred to as Geiger-mode APDs (G-APDs) or Single-photon avalanche diodes. Since the avalanches of G-APDs are self-sustaining a quenching resistor has to be connected in series to each G-APD in order to stop the avalanche. The quenching resistor decreases the bias voltage to a point where the G-APD returns to its initial state since the increased current by the avalanche increases the voltage at the resistor.

SiPMs consist of many cells where each cell contains a G-APD and a quenching resistor. Those cells allow single photon counting. A schematic of a SiPM can be found in Figure 3.3. Though SiPMs offer a promising way to detect photons their greatest disadvantage are noise phenomena. Especially distinguishing signals from dark counts caused by thermal noise, optical crosstalk and after-pulsing are challenges to meet. Thermal noise signifies the creation of electron hole pairs by thermal excitation and optical crosstalk is the recombination of electrons to photons which can happen during one avalanche.

When the SiPMs used for FAMOUS (Hamamatsu S12573-100X) are operated at the recommended over-voltage of $v_{ov} = 1.4\,\mathrm{V}$ the probability for optical crosstalk amounts to $p_{ct} = 35\,\%$ [14]. Afterpulsing is the process of electrons getting captured into the silicon lattice due to impurities of the material. Those electrons are released to a later time causing a second breakdown of the SiPM cell. This is effect is close to be negligible since its probability is below one percent.

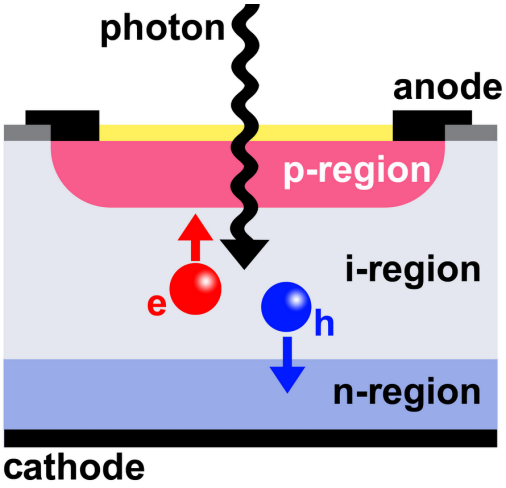

Figure 3.2: Processes within an avalanche photo diode when a photon excites an electron. Adapted from [16].

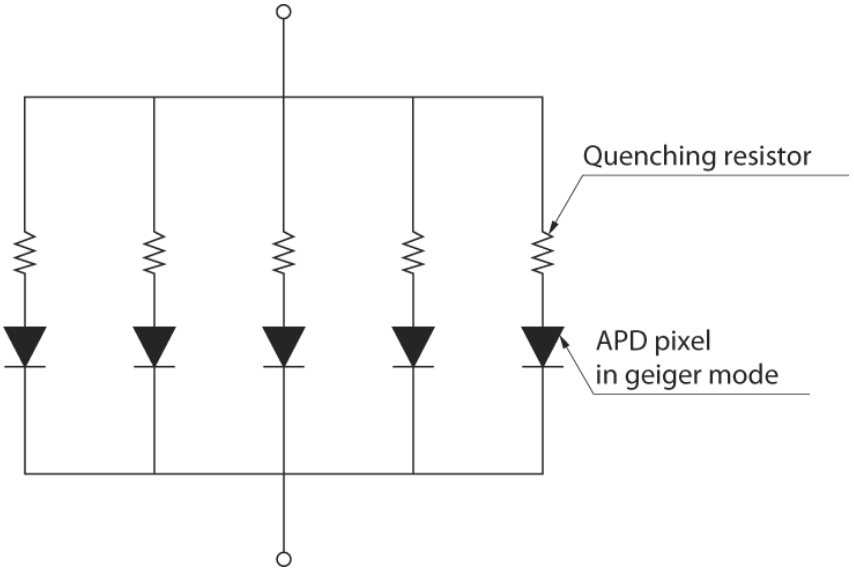

Figure 3.3: Equivalent circuit diagram of a SiPM array. Adapted from [17].

4. Triggerlayouts

For the implementation of a PCB that allows the connection and read out of the new data acquisition system TARGET, trigger groups consisting of four pixels each, have to be chosen. Therefore, a satisfying layout, that meets several requirements is needed. One of which is the symmetric arrangement of each trigger-group on the hexagonal grid. This is especially important at the center of the camera since there is the most precise detection possible. If the arrangement of trigger groups is not symmetric the dead area increases and as a result the sensitivity decreases. Another important aspect is the general trigger group orientation which plays a major role when it comes to systematic effects.

4.1 Drafts

The creation of the first drafts themselves reduces its difficulty to the following problem: How to fill an order 5 hexagon made of 61 tiles (respecting the blind pixels) with groups of four in the most symmetrical way?

This isn't possible in the first place since FAMOUS has three blind pixels thus means one of the 61 pixels always remains unused in the layout, making it impossible to find an ideal solution for the described problem. The hexagon has to be filled with groups of four pixels each because of the data acquisition that uses the sum of four channels as a trigger, only two arrangements can be found which are symmetric. The hexagon to which references are made and which also represents the basis for all layouts is shown in Figure 4.1 Concerning the trigger groups only three optimal arrangements of four pixels can be found that result in a symmetrical structure. Those arrangements are the most compact and balanced for padding the area. They can be found in Figure 4.2. Since its not possible to fill the hexagon using only these arrangements, others inter aria asymmetrical, have to be used. Those are mostly used for the edges of the hexagon due to the lower sensitivity and higher inaccuracy. This leads to the conclusion that all layouts are a compromise between a maximum amount of symmetry and the consideration of all requirements.

Taking account of those aspects three promising layouts were created. Those can be found in Figure 4.3a, 4.3b and 4.3c. The different colours represent the elements of each trigger-group and try to visualise the symmetric and asymmetric parts of a layout. The tiles coloured in white represent the blind pixels and the pixel that is left unused in the layout.

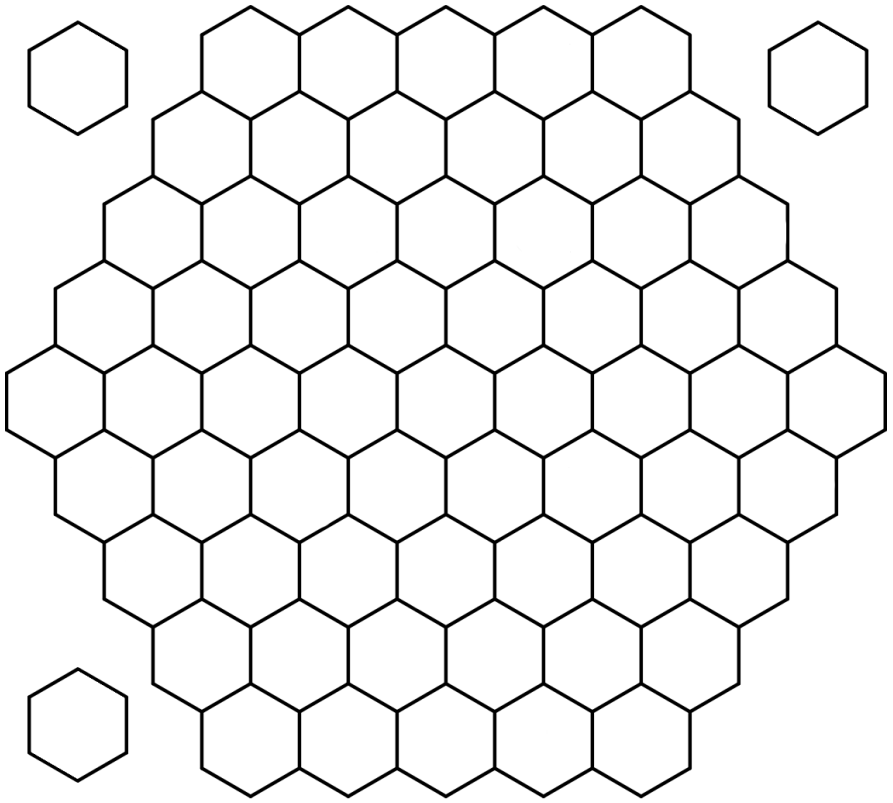

Figure 4.1: The hexagonal structure, where trigger groups of four tiles each have to be found and arranged.

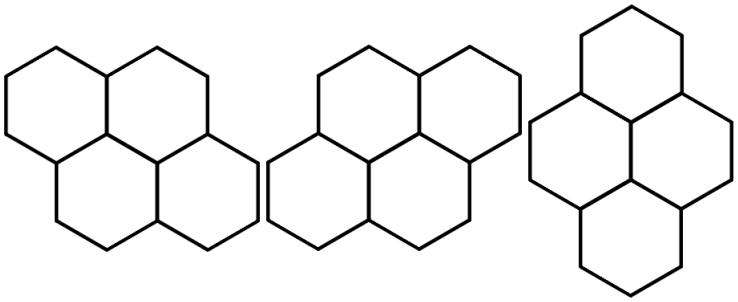

Figure 4.2: Optimal trigger-group arrangements for padding the hexagon. All variations are obtained by combinations of mirroring and rotating of right-most arrangement.

The first layout shown in Figure 4.3a places a special focus on achieving a mostly symmetrical padding of the area around the central pixel (see pixel no. 31 according to Figure 4.1). Therefore only one of the structures shown in Figure 4.2 was used. Accordingly the edges of the hexagon have to be filled with arrangements that differ from the ones shown in Figure 4.2. Those arrangements do not offer a great symmetry or reduction of the dead area but they have to be used to achieve a fill of the complete area.

(a)

(b)

(c)

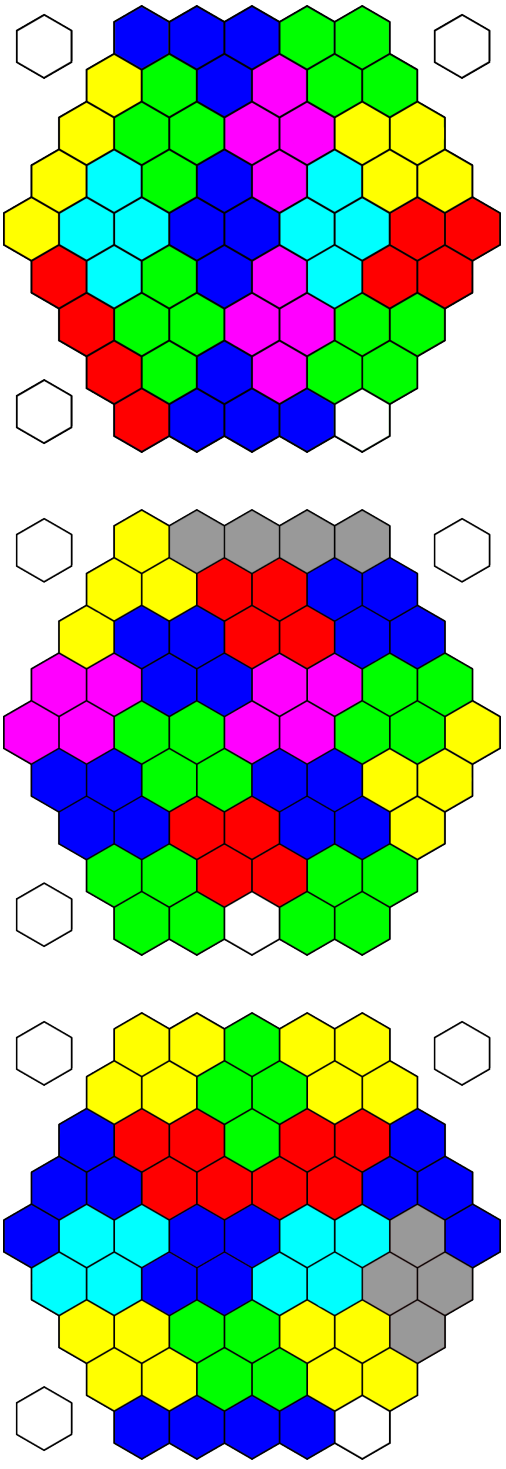

Figure 4.3: Comparison of all layouts. Each group of four tiles with the same colour represents one trigger group. The different colours were used in that manner to highlight visible symmetries. The three blank tiles in the upper and lower left and upper right corner visualise the blind pixels of the FAMOUS telescope.

The aim behind the creation of the second layout, which can be found in Figure 4.3b, was to find a padding that uses a minimum amount of trigger-group arrangements that differ from the ones shown in Figure 4.2. This was basically reached by using only the two mirror-inverted arrangements from Figure 4.2. The remaining area was filled with three trigger-group arrangements, which are at variance from Figure 4.2.

The third layout shown in Figure 4.3c is primarily a variation of the second layout since only two trigger groups were changed to the most-left arrangements from Figure 4.2. The three not perfectly symmetric arrangements from the second layout were moved to different positions to achieve a mostly unidirectional orientation of trigger groups per two rows of pixels.

4.2 Centroids of area

In order to find the best of the three layouts using graphic and geometric tools the centroids of area and the general orientation of the trigger groups has to be scrutinised. These methods reveal the symmetry from a different perspective and provide criteria for finding the best possible layout. To study the symmetry the centroid of each trigger group was determined and then connected with all direct neighbours. This results in a structure with triangular tiles similar to a grid. Comparing the area and shape of the tiles gives clear indications about the distribution of the trigger groups on the hexagon.

The centroids of area of the first layout which can be found Figure 4.4a reveals an area where each triangle has the same shape and surface area (see the greenish highlighted edging of the corresponding trigger groups in Figure 4.4a). That means within a circle around this area the detection is most sensitive and precise. Three very similar areas can be found when bordering three of the remaining centroids in the same way (blueish, reddish and yellowish highlighted edging in Figure 4.4a). Those are not as symmetric as the greenish edged area but they nevertheless provide a reasonable compromise. This becomes even clearer when the similarity of the area around each centroid is compared among each layout. Essentially, only the triangles on the left side vary widely in size and appearance from the others.

The second layout (Figure 4.4b) does not have any areas that can be examined for their similarities. The structure and size of each area varies widely and there can not be found any systematic between the arrangement of the centroids. The area around the centre of the hexagon has no even structure thus essentially reducing the sensitivity of the most important area. Also the sizes of all triangles differ extensively among each other.

A very similar situation can be found when examining the third layout (Figure 4.4c). All triangles do have different sizes and do not create any comparable areas. As in the case of the second layout the central area is not filled with even structures, resulting in a semi optimal layout regarding the analysis of the centroid of area.

(a)

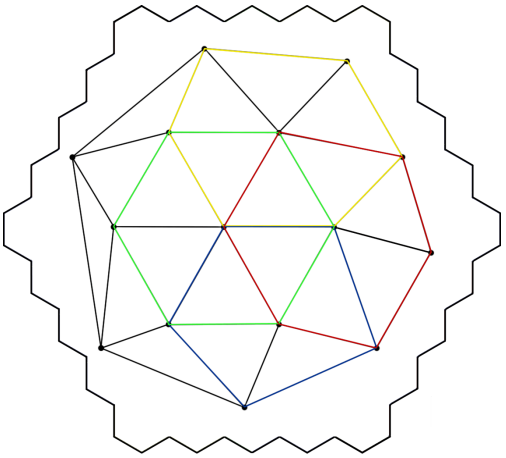

(b)

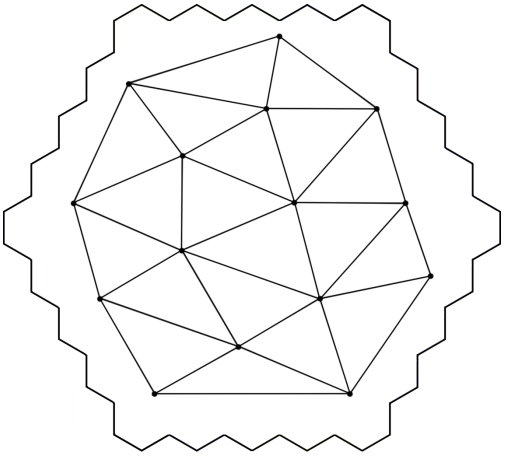

(c)

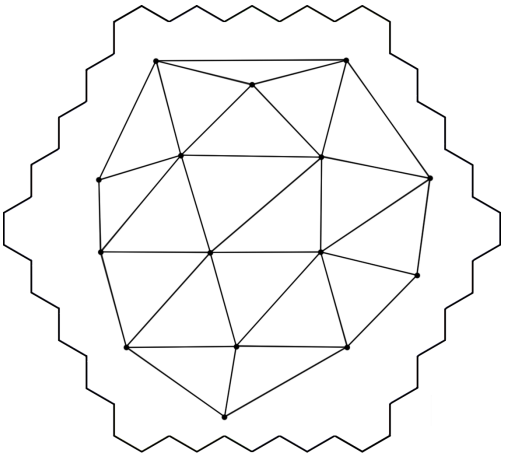

Figure 4.4: The connected centroids of area of all layouts.The centroids were connected in order to reveal the distribution of trigger groups on the hexagonal map. The tiles of the first layout, which are bordered in green, red, yellow and blue highlight areas that are very similar to each other in terms of size and structure.

The interim conclusion for the study of the centroid of area is that the first layout has the most similar filled area compared to the other two layout. This is mainly due to the fact that the centroids of the second and the third layout do not create any comparable areas. Whatever these studies have made abundantly clear that the first layout offers a very special structure and a very balanced arrangement of the trigger groups around the central pixel.

4.3 General trigger group orientations

The goal of the examination of the general trigger group orientation was the creation of a study of the general preferred direction of all layouts and their trigger group orientations. This is especially important since the incident photons arrive under very different angles thus the orientation of every single trigger group plays a non negligible role. A ideal layout should not have a preferred direction because in this case the sensitivity is equal for any angle of incident photons. However the optimal trigger groups presented in Figure 4.2 and any asymmetric arrangement has a certain preferred direction. Therefore it is not possible to vectorially add all directions, so that the sum results in a null vector. The facts, that each differently orientated trigger group may result in systematic effects in the data of the corresponding trigger group channels and that systematic effects may differ for every direction, leads to the conclusion that the exact consideration of all orientation dependent effects is not possible without further investigation. For this reason the second best layout would be such with just one preferred direction, because if systematic effects due to the orientation occur, these would be present in the data of all channels. The correction of this data would be easier than the one with contrarily orientated trigger groups. To visualise the orientation of all trigger groups lines were used. In order to show the general preferred direction of a layout an arrow was used, whereby the orientation of this arrow is according to two reference directions in the x- and y-axis. The reference direction of the x-axis is an arrow point to the right side of the layout and the reference direction of the y-axis is an arrow pointing straight upwards. The trigger group orientations of any trigger group arrangement that differs from the ones shown in Figure 4.2 are deliberately not drawn in.

The general trigger group orientations of the first layout shown in Figure 4.5a is obviously one arrow pointing upwards just like the arrows in the area around the central pixel. If the two arrows on the left side and the four arrows on the right side of the layout are vectorially added this results in one straight arrow pointing upwards. So in total the general preferred direction of this layout is parallel to the reference direction. Since the arrows which do not point straight upwards are located at the left and right edge of the layout this results in an central area that is filled with only unidirectional orientated trigger groups. Therefore detection without any direction dependant systematic effect is most likely possible.

(a)

(b)

(c)

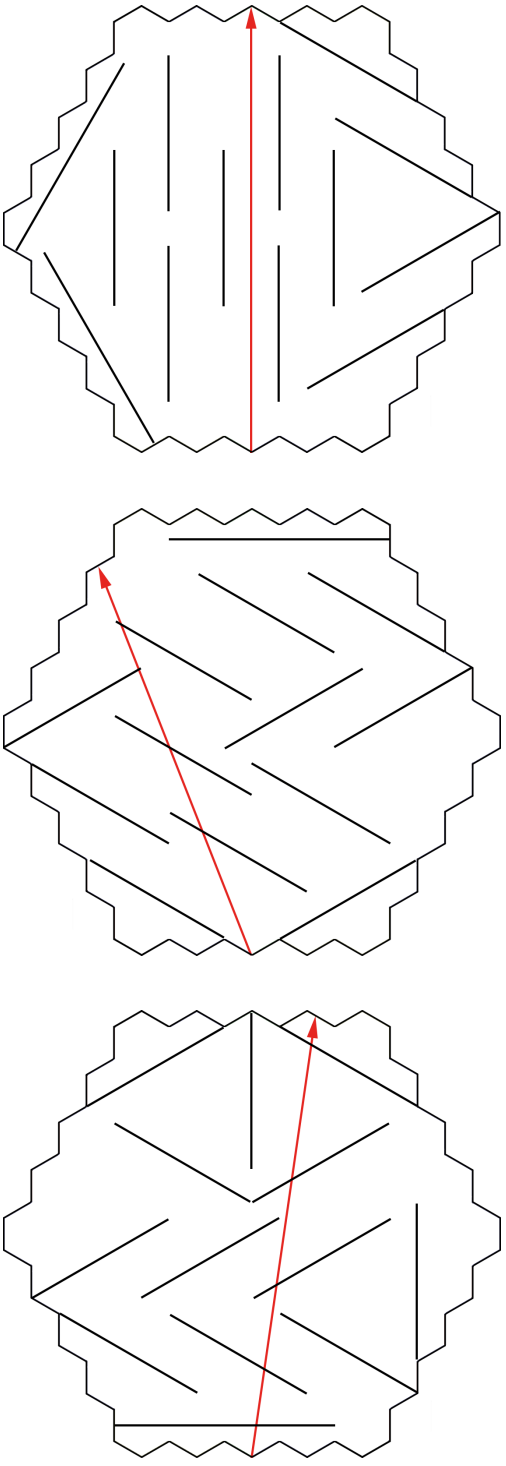

Figure 4.5: The trigger group orientations of all layouts. Each line represents the preferred direction of one trigger group and the red arrow shows the general direction of the total layout, which is received through vecotorially adding all directions of one layout. Any trigger group which differs from the ones shown in Figure 4.2 is not drawn in for reasons of clarity.

The second layout and its trigger group orientations are presented in Figure 4.5b. When looking at the general preferred direction of the layout it turns out that the direction is describable by an arrow that points towards the upper left side. However this is accomplished through a non homogeneous arrangement of differently orientated trigger groups and therefore the central area is not filled by unidirectional orientated trigger groups. This has the consequence that systematic faults within this region may occur and affect the sensitivity. For this reason the arrangements do not offer a satisfying approach for a layout that should be implemented.

The general trigger group orientations of the third layout are presented in Figure 4.5c. The preferred direction of the whole layout is describable by an arrow that points towards the upper right side of the hexagon. In this case the preferred direction was achieved through the usage of trigger groups that in total add up to an upwards pointing arrow, but the trigger group at the lower end of the hexagons shifts the general preferred direction to the right side. Therefore the influence of systematic effects is greater than that of the first layout. In addition, the central area is not filled with unidirectional orientated trigger groups and as result of this the sensibility may decrease.

The final conclusion when looking at the results of the different approaches to obtain a qualitative assessment of the layouts, is that the first layout is certainly the most balanced layout. In all cases it comes closest to meeting the requirements of each focus of study.

5. Simulation

In order to obtain quantitative assessments about the layouts presented in section 4.1 a simulation was written utilising the programming language Python. The simulation should identify differences and advantages between the layouts. Based on this the most efficient layout shall be determined.

5.1 Parameters & Setup

The simulation focuses on Cherenkov showers which are created by a bivariate normal distribution. Figure 5.1 shows a exemplary bivariate normal distribution for an air shower having its mean in the central pixel (x=0, y=0) of the camera. The x- and y-coordinates were assumed independent with the same standard deviation $\sigma_{\mathrm{x}} = \sigma_{\mathrm{y}} = 2r$, where r represents the pixel radius. This values were used during the complete simulation. The corresponding hits map in counts of photons is shown in Figure 5.2. For the purpose of a quantitative evaluation it is necessary to make simplifying assumptions:
To reduce the total amount of calculation time all camera pixel were assumed to be punctiform, therefore the probability to hit a certain pixel was assumed to be the probability to hit the corresponding coordinate according to the value of the probability density function (PDF) at this point. This assumption is legitimate since all pixels have the same size and are therefore scalable to any size. This does not highlight any differences between the layouts, if the air shower is scaled by the same factor. Furthermore the photon detection efficiency (PDE) of all pixels is the same and assumed to be 100%. Since the simulation focuses on the determination of the most efficient layout, especially for the detection of Cherenkov showers, any differences within the detection efficiency would only add systematic effects and reflect the efficiency depending on this systematic effect.
By means of the simulation a evaluation of the number of trigger groups, that are hit by enough photons to exceed the threshold depending on that threshold, is possible. Therefore air showers with randomly chosen centres are simulated, whereby each centre can be one of the 61 pixels of the camera. Subsequently the probability of hitting each pixel is retrieved based on the bivariate normal distribution and its prior chosen centre. The number of photons per pixel is then retrieved by multiplying the probability with the number of photons per simulated shower. During the complete simulation this number was set to a constant value of one million photons per air shower. Based on the allocation of the pixels to trigger groups given by the layouts the sum over the number of photons of the corresponding pixels was calculated.

This results in an array of fifteen numbers per layout, which is then saved for later use. For every shower this process is repeated and the new data is appended to the data of the previous shower. So the total result is an array with a length of the number of simulated air showers and each element of this array consists of a length three array where the amount of detected photons for each trigger group and layout is saved. Based on this array a iteration over different thresholds was started and the number of trigger groups per layout exceeding the current threshold was counted. The threshold represents the signal/noise ratio in number of photons and was increased from 0 to 120000 photons with step widths of one photon per iteration.

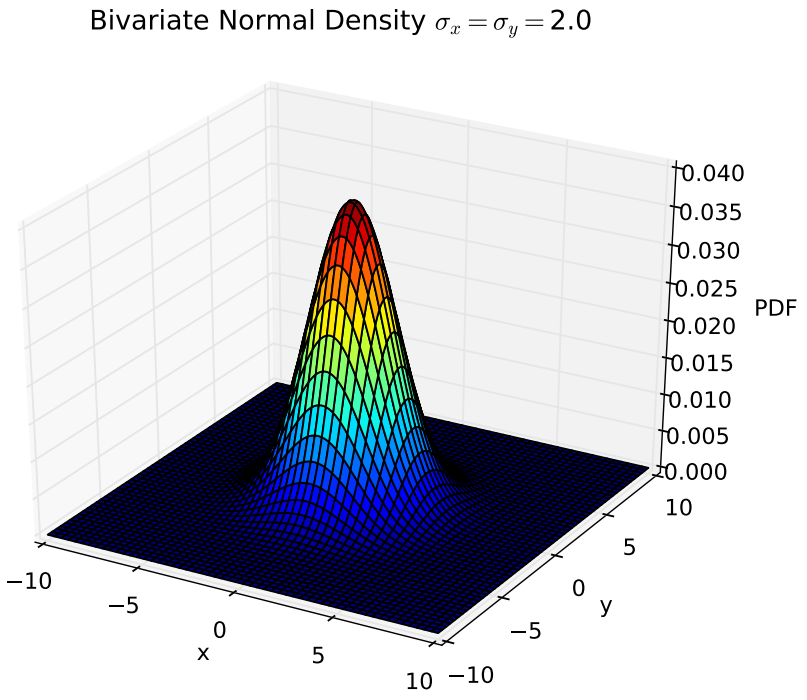

Figure 5.1: Probability density function (PDF) of the bivariate normal distribution used to generate air showers hitting the 61 pixel camera with $\sigma_x = \sigma_y = 2r$. This Figure is an example for an air shower with its mean in the central pixel.

5.2 Results & Conclusion

Based on the approach described in the previous section two plots were created, which plot the total number of trigger groups exceeding the threshold against the corresponding threshold. The first plot can be found in Figure 5.3. It becomes clear that the efficiency differences between each layout are generally not very significant at first glance. Since all graphs are basically lying on top of each other the development of the curve towards greater thresholds is particularly interesting.

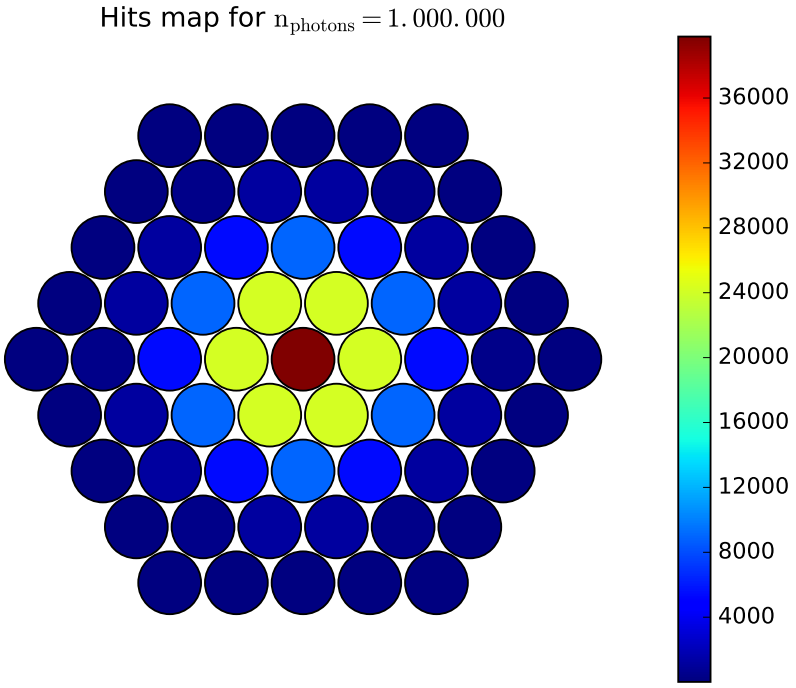

Figure 5.2: Corresponding hits map of the camera according to the PDF shown in Figure 5.1.

When considering the different courses the third layout strikes out because its detection efficiency is better than the one of the other two layouts, when reaching the highest threshold. The minimum number of trigger groups detecting an air shower was reached when the threshold was set to 112186 photons. At this point 199 trigger groups of the first, 209 trigger groups of the second and 194 trigger groups of the third layout were exceeding the threshold. Taking the first layout as a reference this implicates that a 5.03% larger number of trigger groups of the second layout are able to detect air showers out of 500 randomly generated ones. However the number of trigger groups of the third layout detecting air showers at that threshold is a 2.51% smaller number than the one of the first layout. In a second approach the air shower means were not created randomly but instead assigned onto each of the 61 pixels of the camera. This is basically a iteration over each of the camera pixels acting as the mean of an air shower. When using many air showers for a simulation based on random values the drawback is that it flattens any features of a curve. Using the prior described method every pixel has the same weighting and major differences are highlighted. The corresponding plot is shown in 5.4. However the plot reveals very little difference between the layouts. If the threshold is below 70000 photons the trigger groups of the first layout detect more or as many photons as the other two layouts, though this fact changes at higher thresholds. The trigger groups of second and third layout are able to detect more photons than the first layout at any point starting at a threshold of about 70000 photons.

Comparing the number of trigger groups detecting air showers at the same threshold as with the first approach, reveals that the trigger groups of the second and third layout detect 8.33% more photons than the first layout.

Considering all the qualitative and quantitative results leads to the following conclusion: Though the first layout does not perform best when considering the results of the simulation it offers significant geometrically and symmetrically advantages over the other two layouts. The second and third layout do not offer such a even distribution of trigger groups when looking at the central area of the camera, therefore they are most likely to cause systematical effects due to the existence of various preferred directions. In conclusion the first layout was chosen to be the one that is going to be used as the allocation for the implementation of the PCB and with that the TARGET data acquisition.

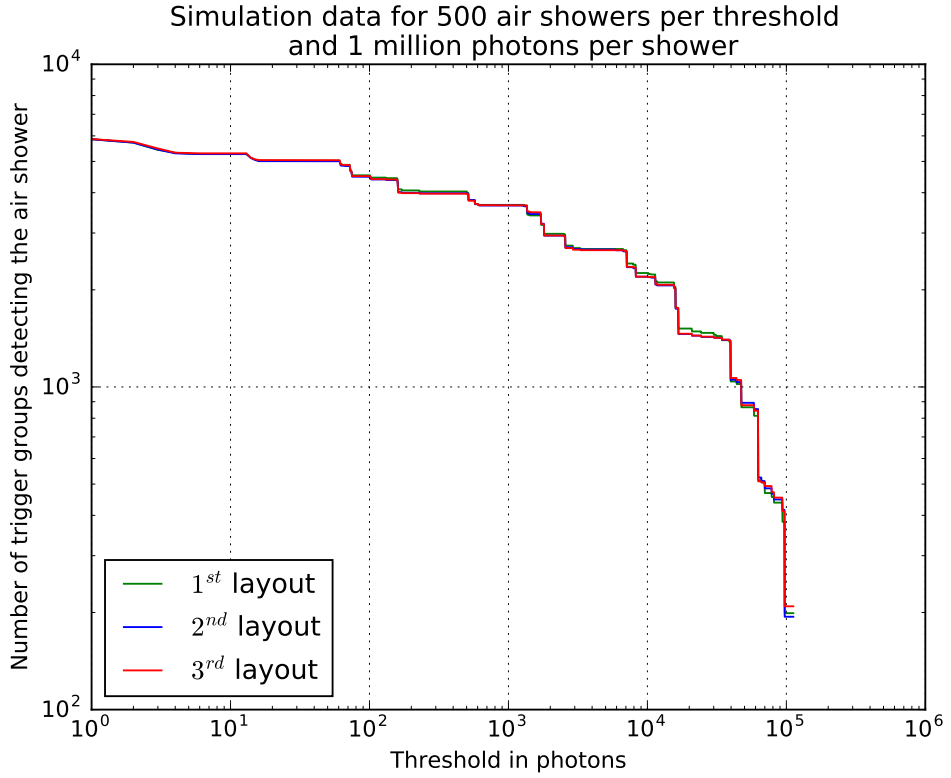

Figure 5.3: The total amount of trigger groups exceeding the threshold plotted against the corresponding threshold. 500 air showers with randomly chosen centres were simulated.

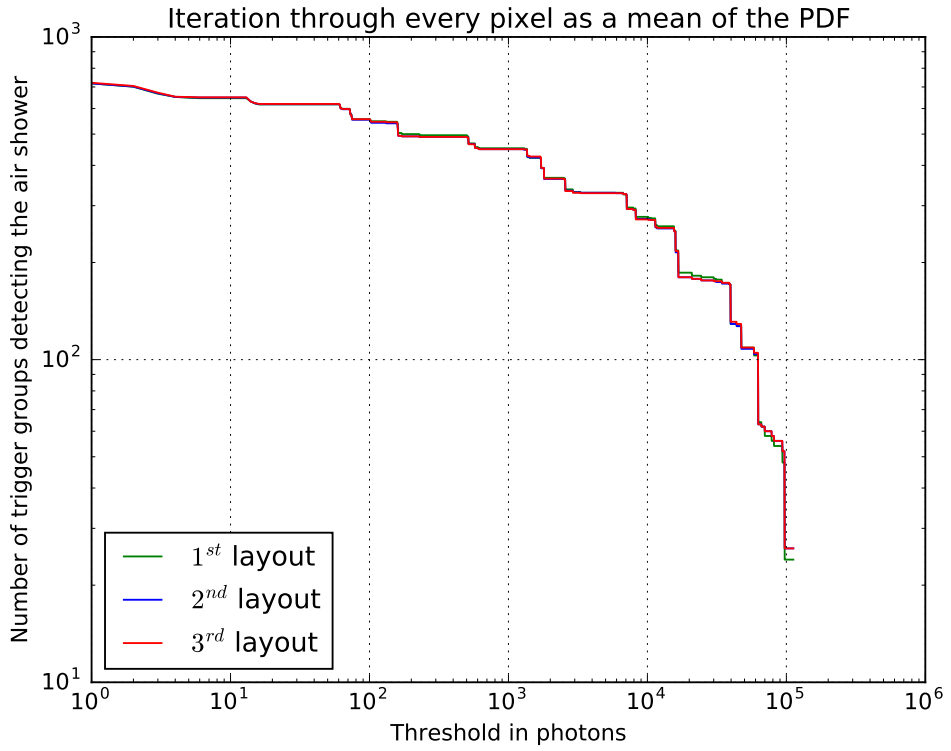

Figure 5.4: Iteration of the centres of an air shower over each pixel of the camera. The total number of trigger groups exceeding the threshold plotted against that threshold.

6. PCB

Based on the results of the qualitative and quantitative evaluation of the three different layouts a PCB (printed circuit board) had to be designed and put into operation. The PCB is going to be connected to the SIPMs of the FAMOUS telescope and the TARGET data acquisition. Therefore the PCB acts as a connecting piece between the telescope and the data acquisition while routing the signals onto four connectors. Whereby each of the connectors forwards sixteen signals, corresponding to four trigger groups.

6.1 Design & Creation

For the creation of the PCB a CAD software, namely TARGET 3001! V18 [18] was used. The assignment of all pixels is predetermined through the trigger groups of the chosen layout, such as the locations of the two 70-pin headers, where the SiPMs are connected to. Since the TARGET data acquisition is connected using four coax cables, the fifteen trigger groups and one group of three blind pixels plus the blank pixel have to be distributed onto four 26-pin connectors. The distribution of the trigger groups was done respecting following conditions:
Trigger groups with signals that are coming from the edges of the 70-pin header were placed at the closest possible location on a connector. This is due to the fact that those signals travelled the greatest distance compared to signals connected to a pin in the middle of the header. This is the easiest way to passively compensate the differences between distances and therewith the signal delay. Another aspect that has been taken into account is the fact that some trigger groups use pixels that are connected to both 70-pin headers. This results in great differences between the connections of the pixels on the PCB. In order to reduce differences to a minimum the affected trigger groups were placed close to the middle, so that the distances from both sides of the 70-pin header are very similar.
When assigning the all pixels onto the four 26-pin connectors, the fifteen trigger groups were assigned first and subsequently the blind pixels and the blank pixel, because they will not act as trigger and therefore the signal delay is not important. In addition to that those pixels were connected to one SMA socket each and then to the empty group of four pins that was left on one of the 26-pin connectors. The additional SMA sockets were installed, in order to provide an additional opportunity to connect to the blind pixels externally, so that noise phenomena can be examined. After the trigger groups were assigned onto the connectors the signals within one trigger group were sorted, so that the amount of vias and the signal lengths were

reduced. In order to connect intersecting signals, vias are used to place the corresponding signal onto a different layer to pass the other signal.

A disadvantage of using vias is the occurrence of electrical crosstalk that can reflect strong signals onto the layer lying above or below. As a last step all signals were connected, whereby this resulted in a first draft version of the PCB layout. Afterwards each signal was optimised, so that the total number of vias is reduced and no ground plane islands occur. Any remaining ground plane island were removed by connecting them to the proper ground.
The final layout can be found in Figure 6.1 and a larger version in A.10. In the upper left and right corner the four SMA socket which are connected to the three blind pixels and the blank pixel are shown. The two 70-pin headers are placed on the left and right side of the layout and are labelled as *IN1* and *IN2*. The four 26-pin connectors are labelled as *OUT1* to *OUT4* and located close to the centre of the PCB. The lines indicate the connections between the 70-pin headers and the 26-pin connectors and the different colours represent the two layers of the PCB.
Upon completion of the PCB the different headers had to placed on the board. Therefore I soldered the two 70-pin headers by hand but the four 26-pin connectors had to placed using a different approach since the contacts of the connector are beneath the component. In order to apply soldering paste to the pads of the four connectors a stencil was used and the four connectors were carefully placed on top of the soldering paste. Subsequently the PCB was put into an oven for the purpose of melting the soldering paste and as result of that the automatically connection of the pads with the contacts. Figure 6.2 and 6.3 shows the front and the back of the PCB before populating the board. The finished board mounted to the FAMOUS telescope can be found in 6.4.

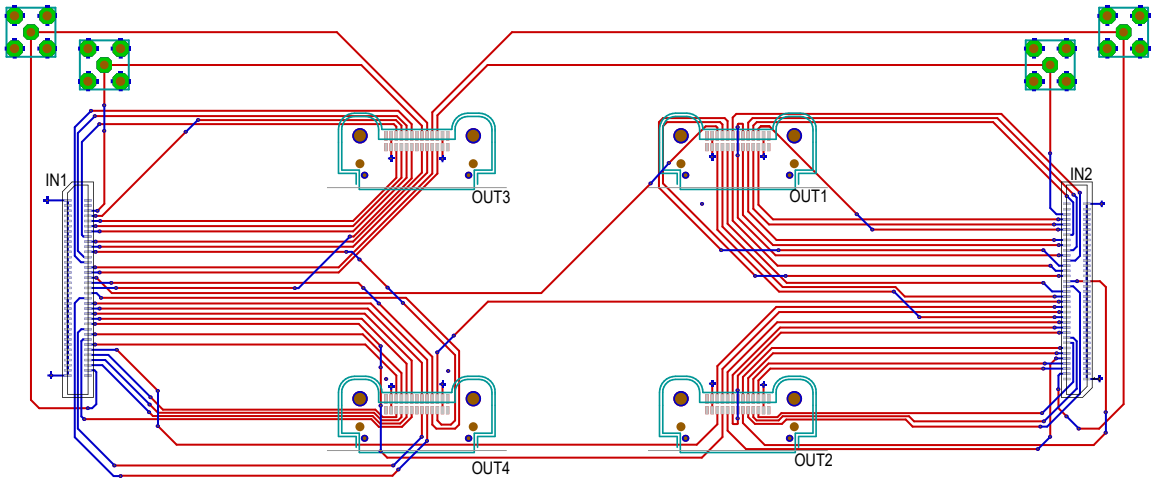

Figure 6.1: Final design of the PCB. The signals are coming from the two 70-pin headers on the left and right side of layout and are labelled as *IN1* and *IN2*. The PCB routs the signals onto four 26-pin connectors labelled as *OUT1* to *OUT4*.

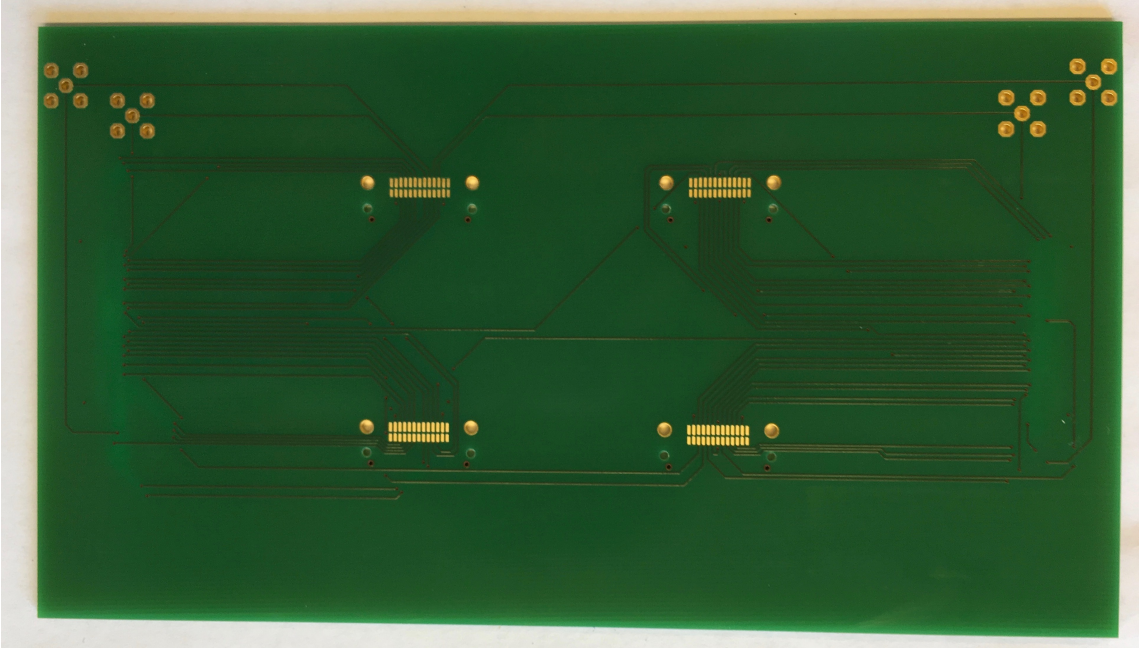

Figure 6.2: Front of the finished PCB.

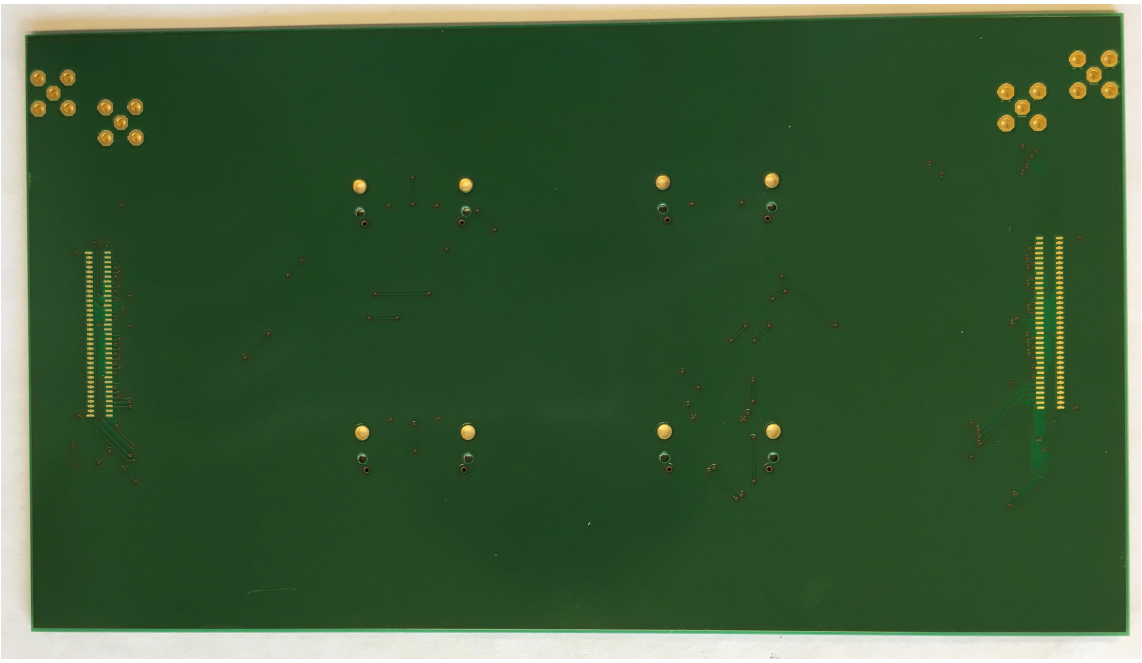

Figure 6.3: Back of the finished PCB.

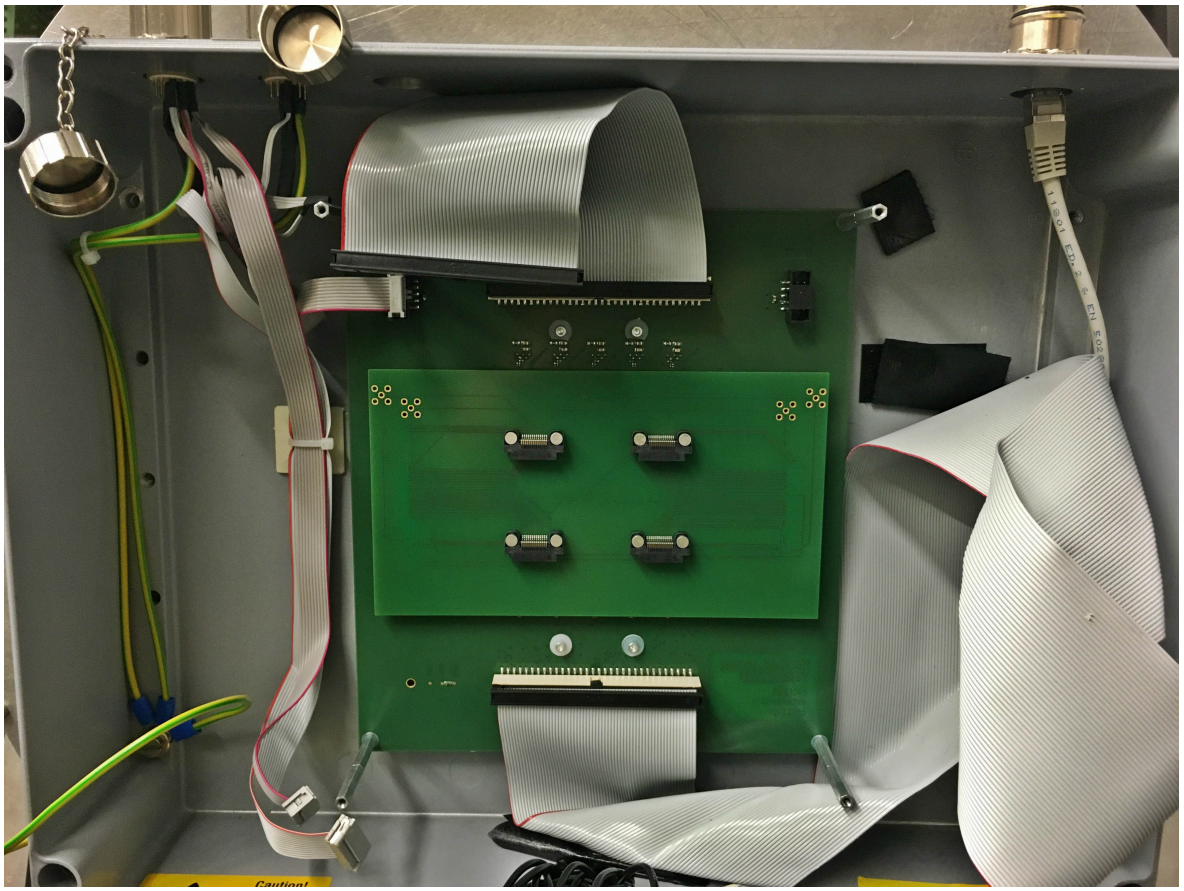

Figure 6.4: The finished PCB mounted to the back of the FAMOUS telescope.

6.2 Measurements & Tests

Before the headers were placed onto the PCB several tests were performed in order to proof the functionality of the PCB. First of all a simple continuity test was performed for the purpose of proofing that the signal assignment is according to the layout. In response, a short-circuit test was executed in order to verify that no signal is connected incorrectly. After the PCB was mounted onto the back of the FAMOUS telescope some basic functionality tests were executed to demonstrate the functioning of all 64 SiPMs on the one had and to proof that the SiPM signals are successfully forwarded using the PCB on the other hand. Therefore every single SiPM was connected to an oscilloscope with the PCB interposed and a dark noise measurement was started. If the characteristic traces during such a measurement were found, this was used as an indicator of a functional SiPM. One characteristic dark noise trace can found in Figure 6.5. During the measurement five channels were found that did not provide any signal of that kind. Therefore the PCB was removed, the issue was investigated and it turned out that some resistors on a existing board, that provides the power for the SiPMs were not soldered completely. Afterwards the measurement was repeated and it was possible to successfully show that all 64 SiPMs are ready to use. Additionally one last cross check was done in the form of proofing the sensibility of the SiPMs, if exposed to a light source. For this purpose randomly

chosen pixels were connected to the oscilloscope and subsequently hit with the light beam of a laser pointer. If a change of the oscilloscope image was observable the SiPM was considered as fully functional.

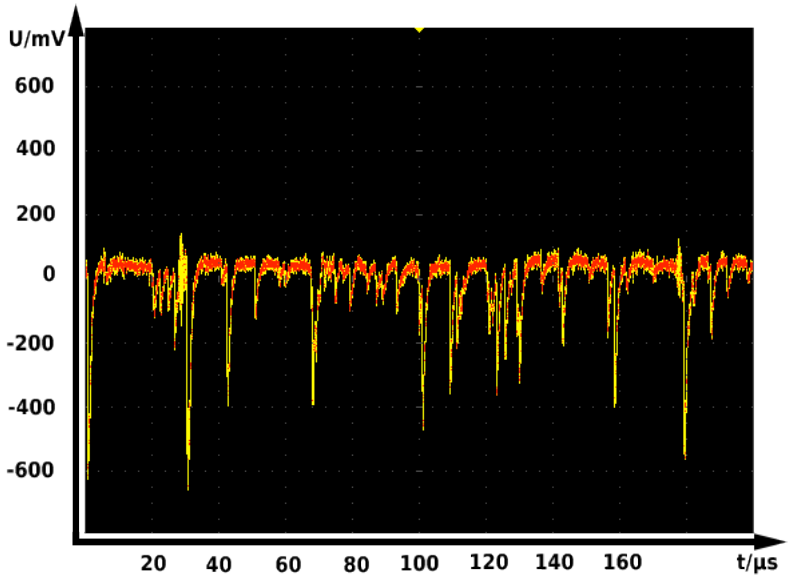

Figure 6.5: Dark noise measurement of one SiPM.

7. Summary and Outlook

In the scope of this thesis, three layouts were created and quantitative and qualitative criteria for weighting those layouts were found. In that manner the qualitative differences were examined with regard to the centroids of area and preferred trigger group directions. It turned out that the first layout has very advantageous properties concerning the qualitative examination of the geometric characteristics. The quantitative examination which was performed in the form of a simulation provided the last criteria to take a decision, which of the layouts is going to provide the pixel assignments for the creation of the PCB. Though the first layout does not perform best in terms of the simulation, the first layout outperforms the other two layouts by far, when looking at the geometric characteristics. Therefore the decision was taken to use the first layout for the implementation of the PCB.
The PCB that connects and routs the signals according to the layout was successfully completed and put into operation. Various tests and measurements were performed to demonstrate the functionality of the SiPMs as well as the PCB. Overall all 64 pixels of the FAMOUS telescope are operational and the data can be read out using the new TARGET data acquisition. Therewith the upgrade of the FAMOUS telescope to a 64 pixel version was successfully completed.

A. Appendix

A.1 All layouts

A.1.1 Drafts

A.1.2 Centroids of area

A.1.3 General trigger group orientations

A.2 PCB

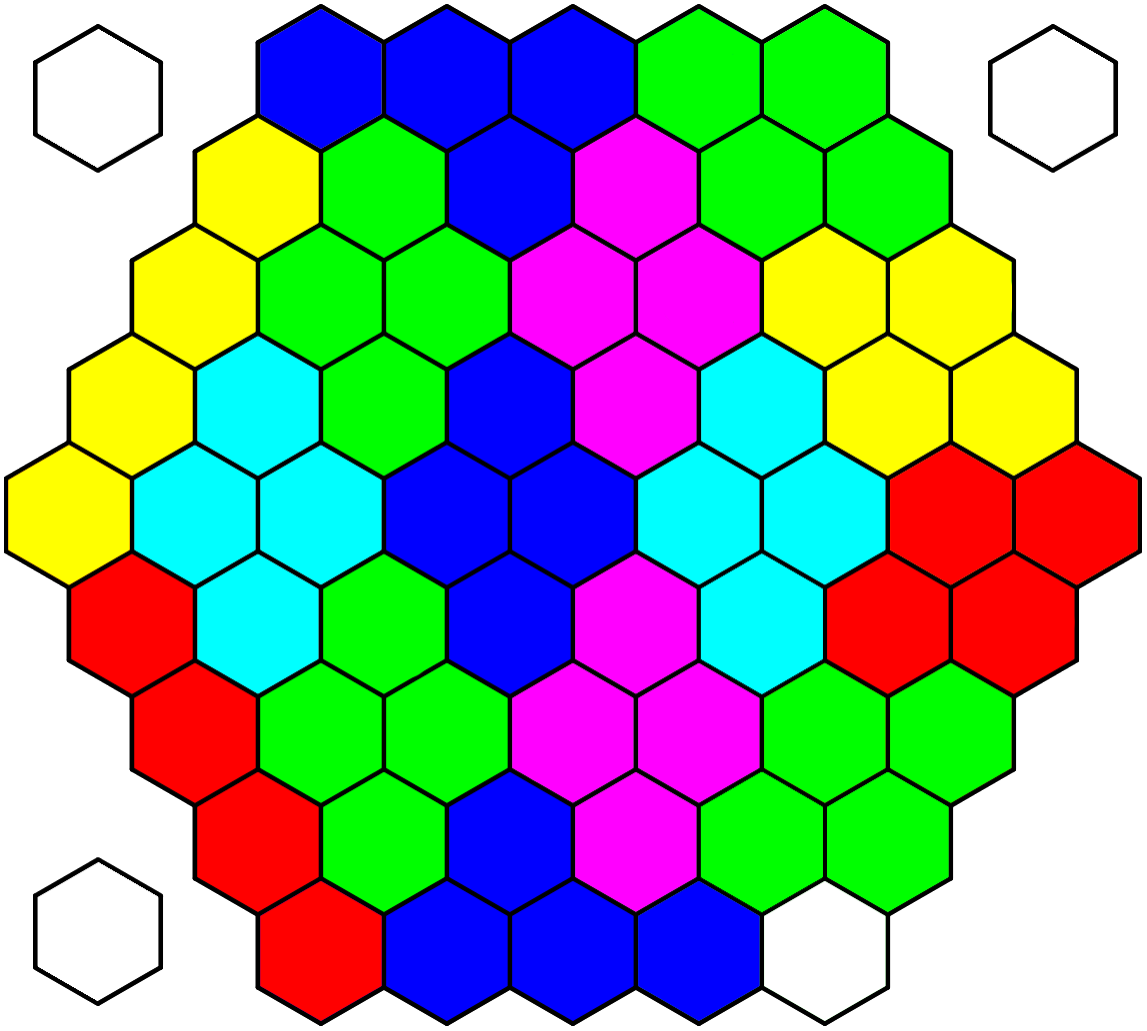

Figure A.1: First layout for the trigger implementation. Each group of four tiles with the same colour represents one trigger group. The different colours were used in that manner to highlight visible symmetries. The three blank tiles in the upper and lower left and upper right corner visualise the blind pixels of the FAMOUS telescope.

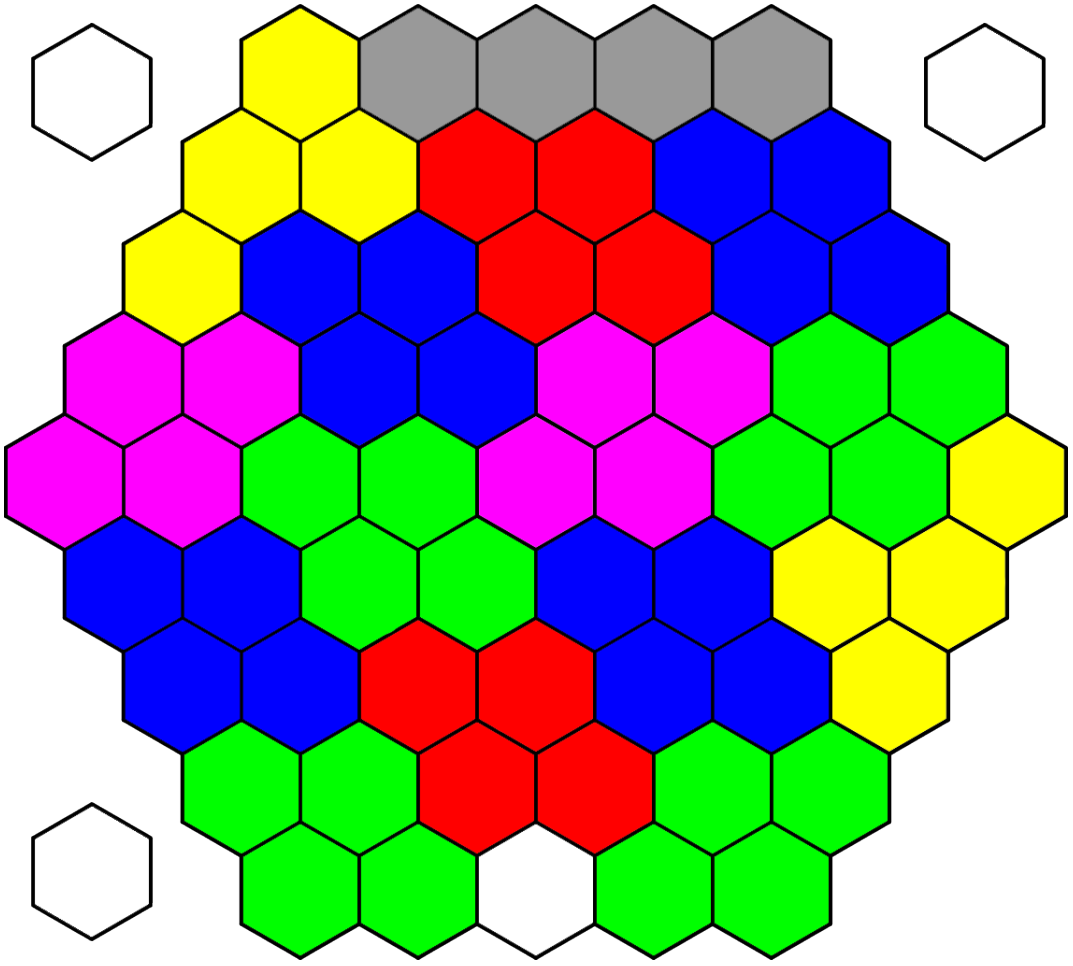

Figure A.2: Second layout for the trigger implementation.

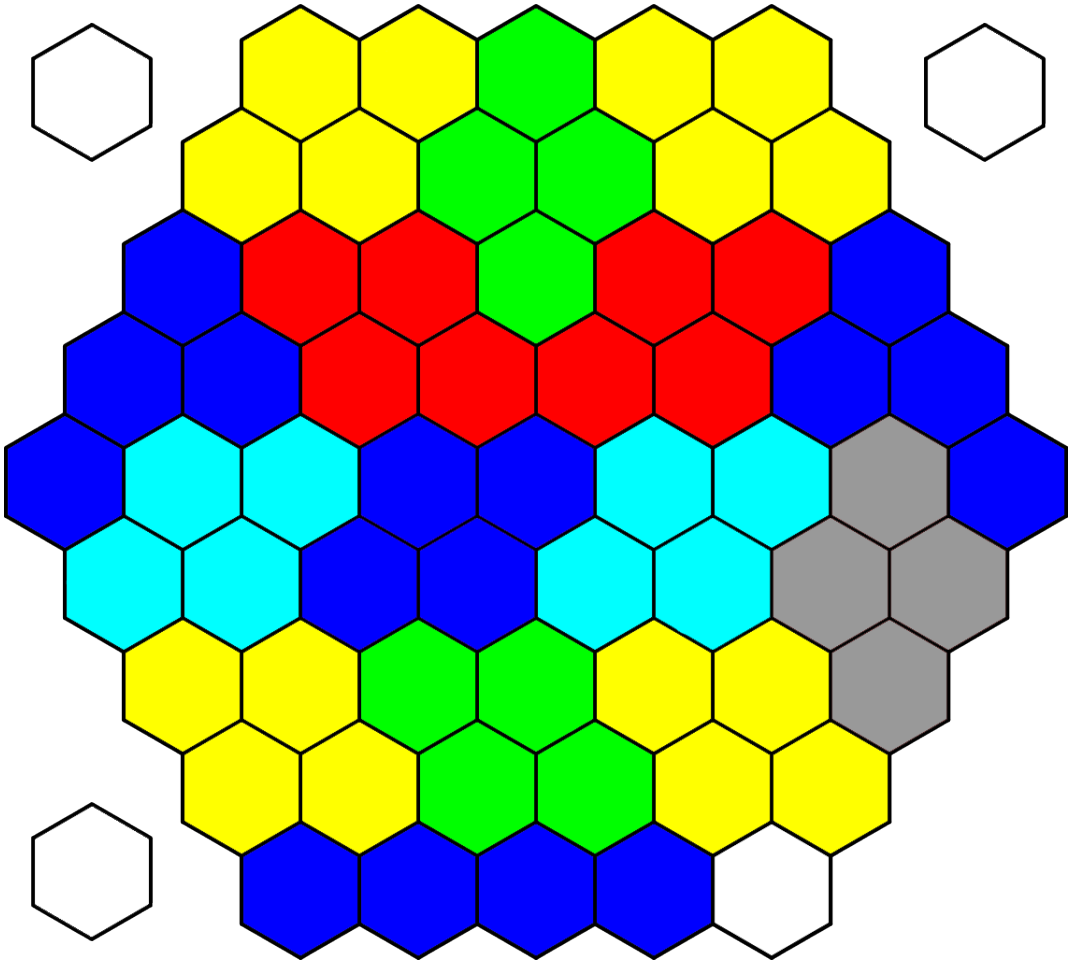

Figure A.3: Third layout for the trigger implementation.

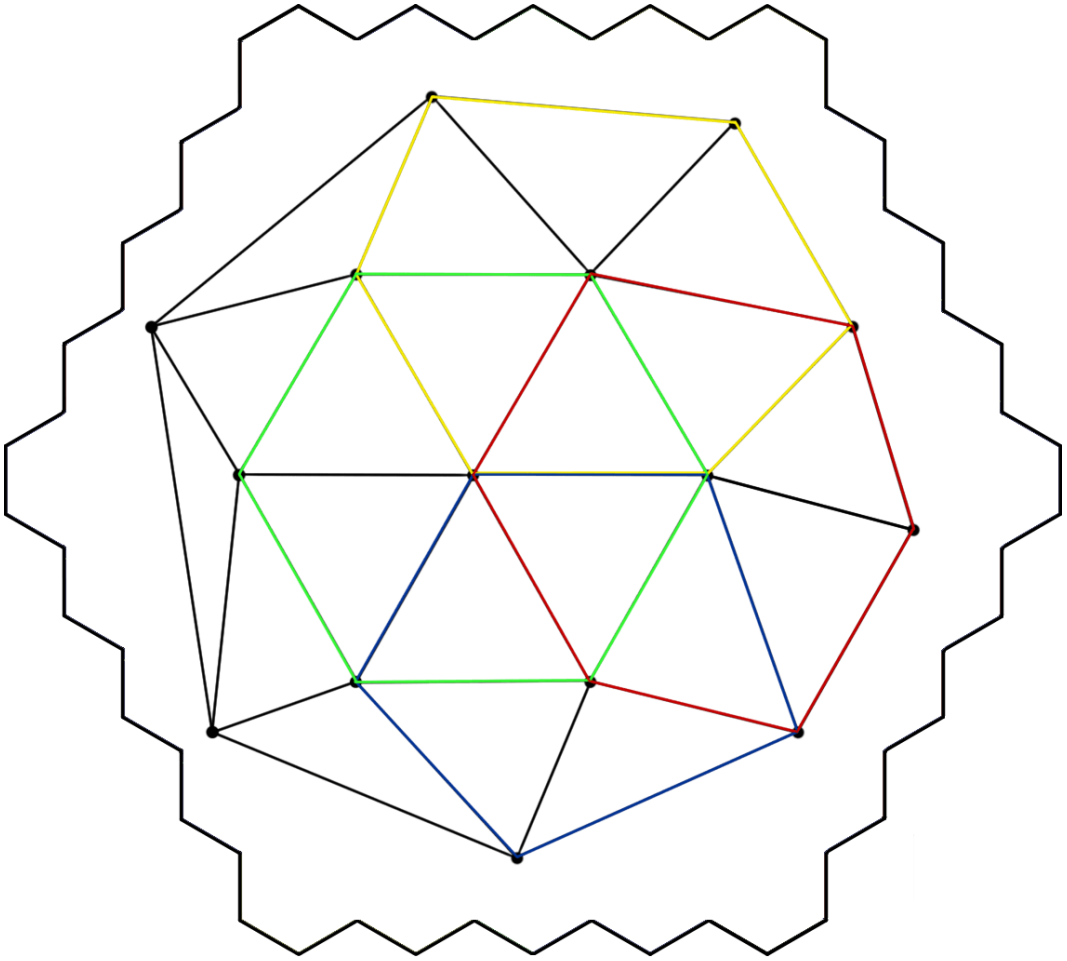

Figure A.4: The connected centroids of area of each trigger group of the first layout. The centroids were connected in order to reveal the distribution of trigger groups on the hexagonal map. The tiles outlined in green, red, yellow and blue highlight areas that are very similar to each other in terms of size and structure.

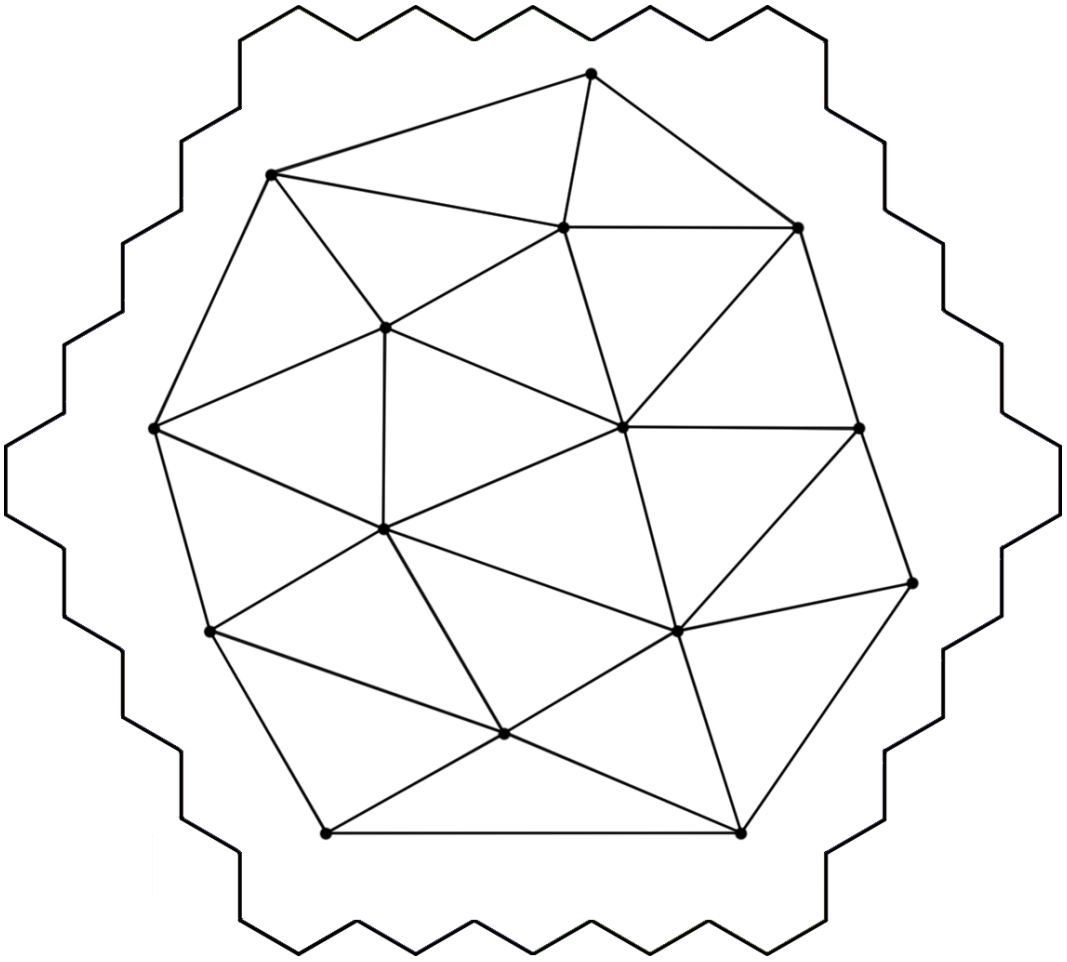

Figure A.5: The connected centroids of area of the second layout.

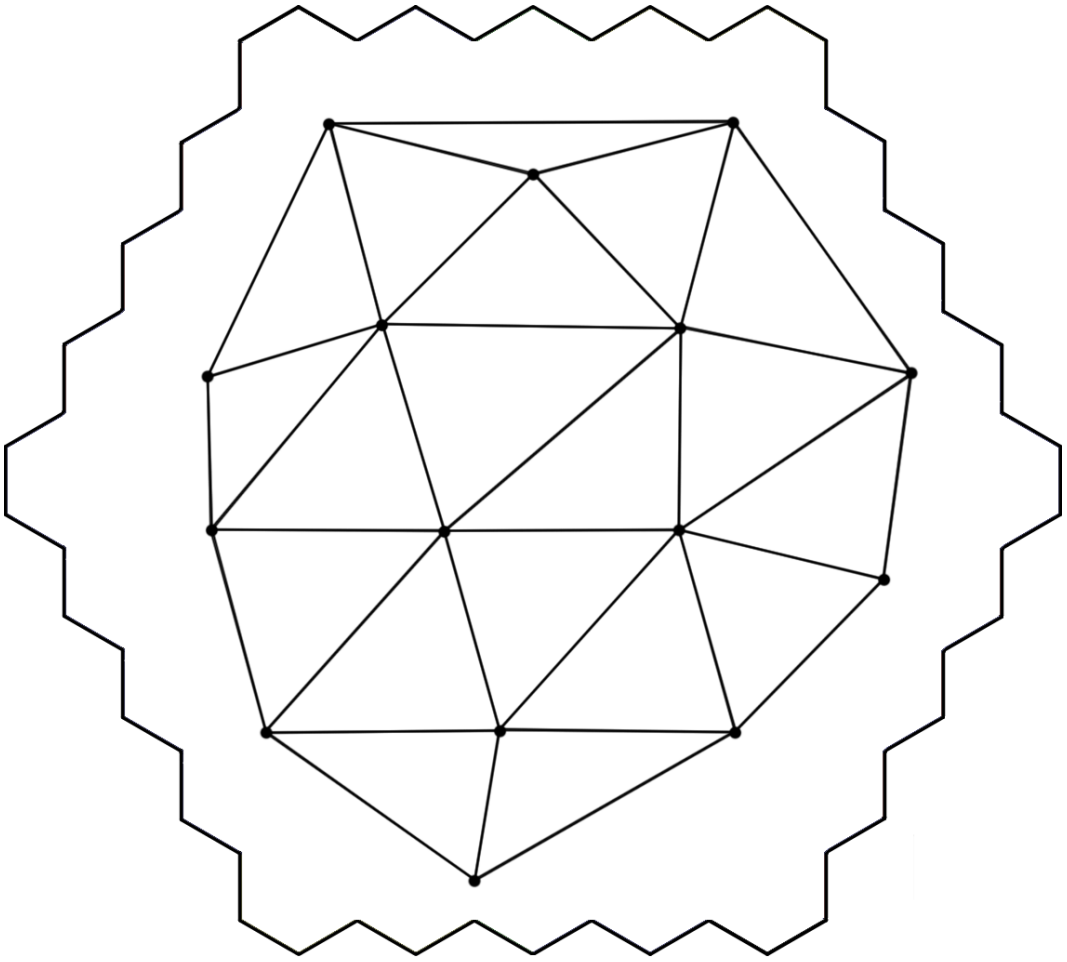

Figure A.6: The connected centroids of area of the third layout.

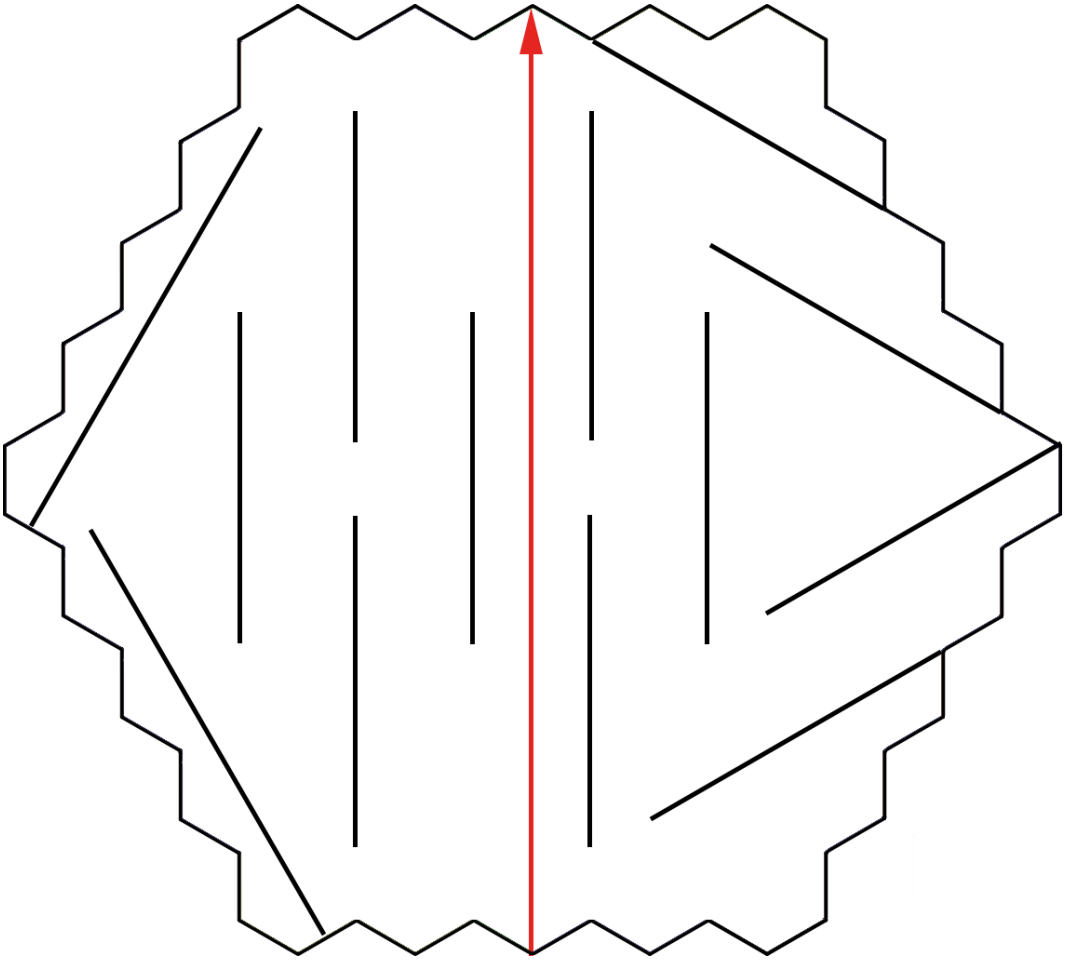

Figure A.7: Trigger group orientation of the the first layout. Each arrow represents the preferred direction of one trigger group. Lines without arrowheads visualise trigger group directions that are perpendicular to the reference direction. Whereby the reference direction was chosen to be a straight upwards pointing arrow. Any trigger group which differs from the ones shown in Figure 4.2 is not drawn in for reasons of clarity.

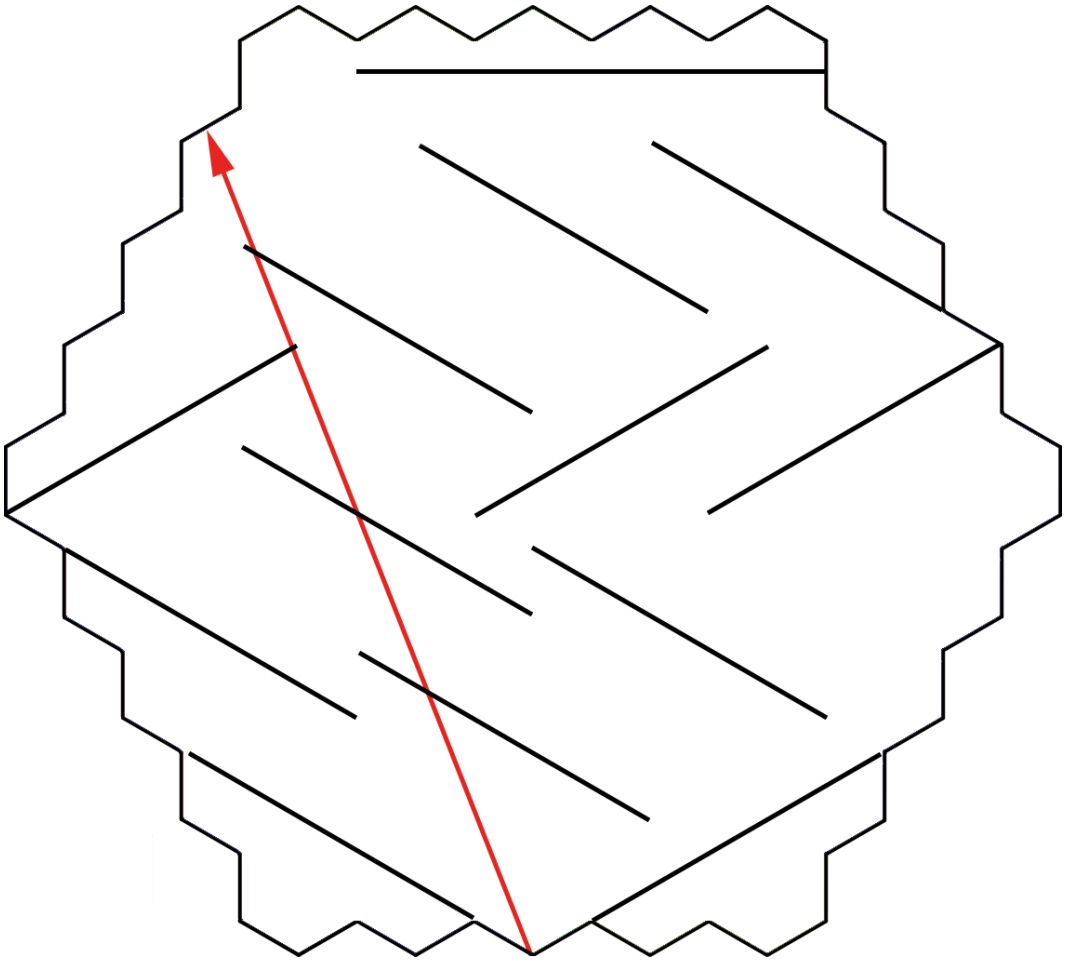

Figure A.8: Trigger group orientations of the second layout.

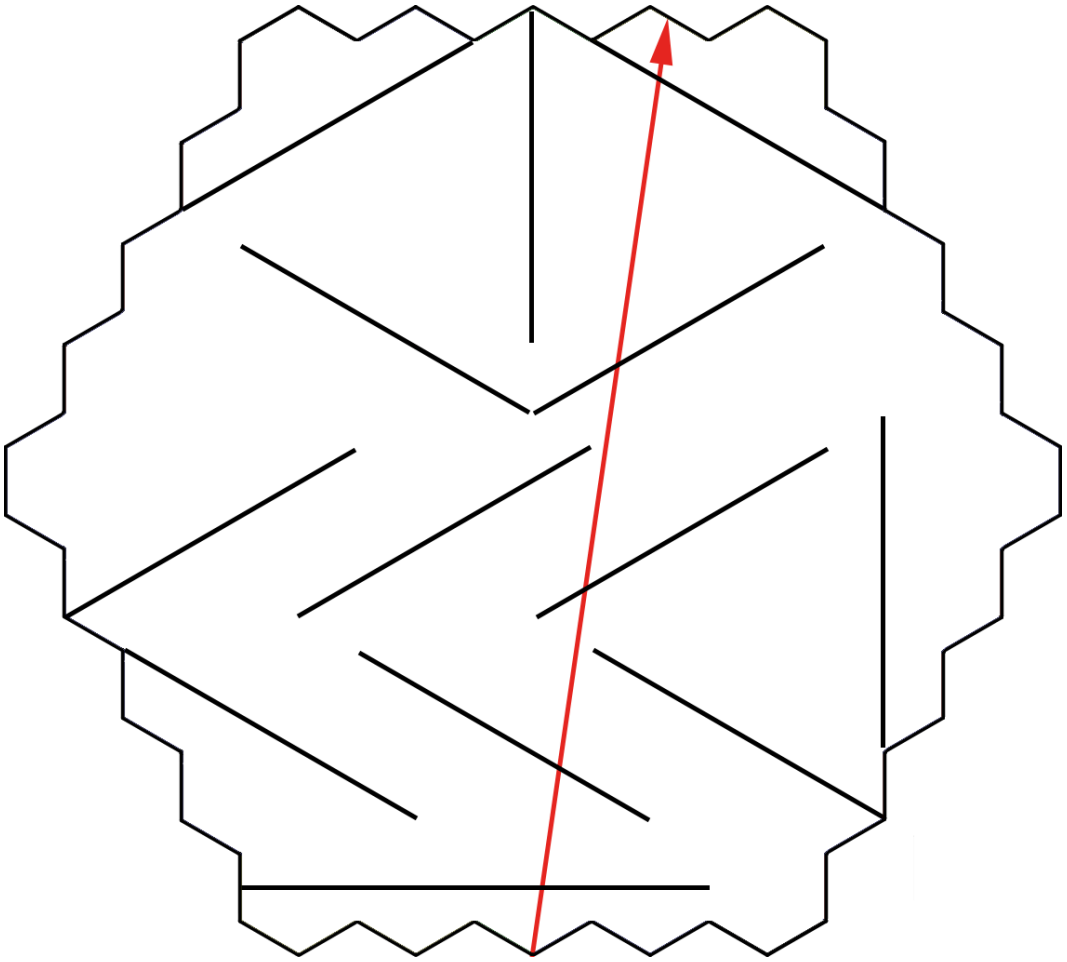

Figure A.9: Trigger group orientations of the third layout.

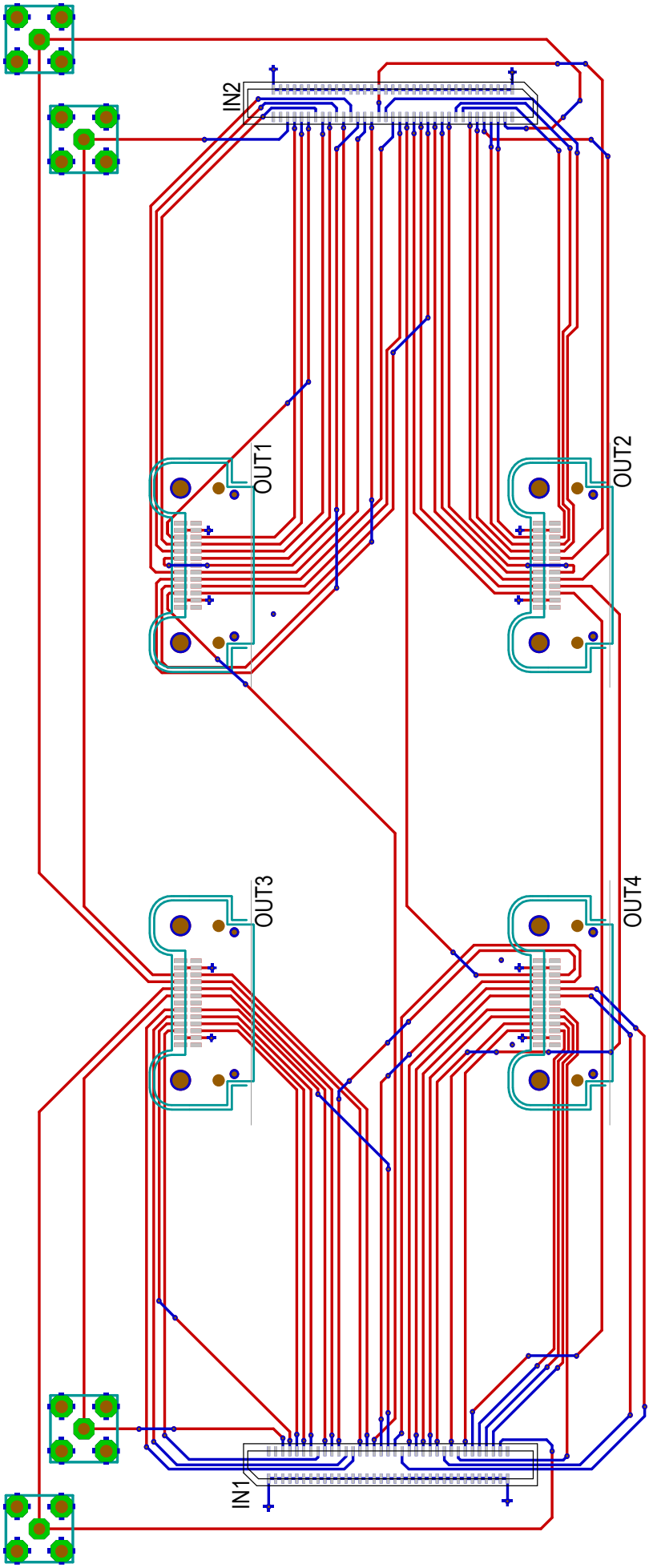

Figure A.10: Final design of the PCB.

Bibliography

[1] V. F. Hess, "Über Beobachtungen der durchdringenden Strahlung bei sieben Freiballonfahrten", *Physikalische Zeitschrift* **13** (Nov, 1912) 1084–1091. [Online; accessed 5-September-2016].

[2] P. Auger, P. Ehrenfest, R. Maze, J. Daudin, and R. A. Fréon, "Extensive Cosmic-Ray Showers", *Rev. Mod. Phys.* **11** (Jul, 1939) 288–291.

[3] **Particle Data Group** Collaboration, J. Beringer *et al.*, "Review of Particle Physics", *Phys. Rev. D* **86** (Jul, 2012) 309.

[4] J. Blümer, R. Engel, and J. R. Hörandel, "Cosmic rays from the knee to the highest energies", *Progress in Particle and Nuclear Physics* **63** no. 2, (Oct, 2009) 21–28, `arXiv:0904.0725 [astro-ph.HE]`.

[5] **The Pierre Auger** Collaboration, J. Abraham, P. Abreu, *et al.*, "Observation of the Suppression of the Flux of Cosmic Rays above 4×10^{19} eV", *Phys. Rev. Lett.* **101** (Aug, 2008) 1–7.

[6] J. Matthews, "A Heitler model of extensive air showers", *Astroparticle Physics* **22** no. 5–6, (Jan, 2005) 387–397.

[7] T. K. Gaisser and A. M. Hillas, "Reliability of the method of constant intensity cuts for reconstructing the average development of vertical showers", *Proc. of 15th International Cosmic Ray Conference* **8** (Aug, 1977) 353–357.

[8] H. M. Eichler, "Characterisation studies on the optics of the prototype fluorescence telescope FAMOUS", *Master's thesis*, *RWTH Aachen* , (Mar, 2014), [Online; accessed 6-September-2016].

[9] K. J. Meagher, "Schwarzschild-Couder Telescope for the Cherenkov Telescope Array", *Proc. SPIE* **9145** (Jul, 2014) 914533–914533–10, `arXiv:1407.3271v1 [astro-ph.IM]`.

[10] M. M. Al-Rubaiee A., Hashim U. and A.-D. Y., "Study of Cherenkov light lateral distribution function around the knee region in extensive air showers", *Serbian Astronomical Journal* **190** (May, 2015) 79–85, `arXiv:1505.02757v1 [physics.gen-ph]`.

[11] P. Kuiper, "Cherenkov wavefront", (Jun, 2007), [Online; accessed 7-September-2016].

[12] **The Pierre Auger** Collaboration, J. Abraham *et al.*, "The Fluorescence Detector of the Pierre Auger Observatory", *Nuclear Instruments and Methods in Physics Research Section A* **620** (Jul, 2009) 227–251, arXiv:0907.4282v1 [astro-ph.IM].

[13] K.-H. Kampert and A. A. Watson, "Extensive Air Showers and Ultra High-Energy Cosmic Rays: A Historical Review", *The European Physical Journal H* **37** no. 3, (Jul, 2012) 359–412, arXiv:1207.4827v1 [physics.hist-ph].

[14] T. Niggemann, "The Silicon Photomultiplier Telescope FAMOUS For The Detection Of Fluorescence Light", *PhD thesis*, *RWTH Aachen* , (Nov, 2016), [To be published in November 2016].

[15] T. Niggemann *et al.*, "Status of the Silicon Photomultiplier Telescope FAMOUS for the Fluorescence Detection of UHECRs", arXiv:1502.00792v1 [astro-ph.IM].

[16] M. Lauscher *et al.*, "Silicon Photomultiplier (SiPM) Characterization for Fluorescence Light Detection", (Sep, 2011), [Online; accessed 12-September-2016].

[17] J. Rennefeld, "Studien zur Eignung von Silizium Photomultipliern für den Einsatz im erweiterten CMS Detektor am SLHC", *Diploma thesis*, *RWTH Aachen* , (Feb, 2010), [Online; accessed 20-September-2016].

[18] Ing.-Büro FRIEDRICH, "Leiterplatten CAD Software TARGET 3001! V18 Design Station", (2016) , [Online; accessed 19-October-2016].

Danksagung - Acknowledgements

Zunächst möchte ich mich bei Jun. Prof. Dr. Bretz und Prof. Dr. Hebbeker bedanken, die es mir überhaupt ermöglicht haben, derartige Einblicke, wie mit dem FAMOUS-Projekt und dessen Bestandteile zu ermöglichen.
Weiterhin möchte ich Johannes Schumacher, meinem Betreuer, danken, der mir jederzeit geduldig und beratend zur Seite stand. Ohne seine Korrekturen, Ratschläge und Anregungen wäre manches Probleme zu einer größeren Herausforderung geworden.
Außerdem möchte ich meiner Familie für ihre moralische Unterstützung und ihren Rückhalt, der bei der Erstellung dieser Arbeit omnipräsent war, danken.
Insbesondere danke ich allen, die mich beim Erstellen dieser Arbeit unterstützt haben und ich versäumt habe, sie hier namentlich zu erwähnen.

Erklärung

Hiermit versichere ich, dass ich diese Arbeit einschließlich beigefügter Zeichnungen, Darstellungen und Tabellen selbstständig angefertigt und keine anderen als die angegebenen Hilfsmittel und Quellen benutzt habe. Alle Stellen, die dem Wortlaut oder dem Sinn nach anderen Werken entnommen sind, habe ich in jedem einzelnen Fall unter genauer Angabe der Quelle deutlich als Entlehnung kenntlich gemacht.

Aachen, den 31. Oktober 2016

_____

Alexander Bogner